

EXPLORATION OF INTERFACIAL THERMAL CONDUCTANCE OF GOLD
NANOPARTICLES USING MOLECULAR DYNAMICS

A Dissertation

Submitted to the Graduate School
of the University of Notre Dame
in Partial Fulfillment of the Requirements
for the Degree of

Doctor of Philosophy

by
Suzanne M. Neidhart

J. Daniel Gezelter, Director

Graduate Program in Chemistry and Biochemistry

Notre Dame, Indiana

October 2018

EXPLORATION OF INTERFACIAL THERMAL CONDUCTANCE OF GOLD
NANOPARTICLES USING MOLECULAR DYNAMICS

Abstract

by

Suzanne M. Neidhart

In this dissertation I present work on elucidating factors important to heat transport in gold nanostructures, particularly nanoparticles, examining the effect of particle size, ligand layer rigidity, and surface gold vibrational freedom. The interfacial thermal conductance of various particles, as well as the thermal conductivity of nanoarrays that are of interest to see trends in heat transport. Direct simulations of interfacial thermal conductance of solvated gold nanoparticles using molecular dynamics were calculated. All particle simulations used the Langevin Hull method for non-periodic systems.

Experimental nanoparticles contain a moiety, or ligand layer, at the surface of each particle that prevents aggregation and is a result of the method used in the formation of the particles. This moiety is essential in controlling movement of heat from a particle to the surrounding media. In particular, the following study looks closely at how the rigidity of this ligand layer and the length of the ligand change thermal transport at the interface of the particle. This allows for further insight into the important factors for ligand and solvent interactions to optimize heat flow. Proposed mechanisms for heat transfer rely on two effects: the vibrational overlap of the materials at the interface and the density overlap of the same materials.

After finding no direct relationship for particle size with the ligand layer and the

thermal transport, a simpler system was examined: bare nanoparticles in solvent. The particles consist of nanospheres, icosahedra, and cuboctahedra. The latter two display facets that are common in many nanostructures due to their stability. The interfacial thermal conductivity (G) of the particles was examined based on radius and particle type. The coordination of gold atoms at the particle surface, giving information about the vibrational freedom, displayed a slight correlation with G . This supports the proposed important factors for heat transport found in the ligand layer work.

Finally, the ideas from both prior works are combined to study $Au_{144}PET_{60}$ particles in isolation and in an array. These small particles ($r \approx 10 \text{ \AA}$) have highly undercoordinated gold atoms within the ligand layer.

CONTENTS

FIGURES	iv
TABLES	viii
CHAPTER 1: INTRODUCTION	1
1.1 Heat Transport	2
1.1.1 Heat Transfer at Interfaces	3
1.1.2 Acoustic Mismatch Model	3
1.1.3 Diffuse Mismatch Model	5
1.2 Molecular Dynamics	7
1.2.1 Representations of Atoms	10
1.2.2 Boundary Conditions	11
1.3 Transport Coefficients	15
1.3.1 Equilibrium Molecular Dynamics	16
1.3.2 Non-Equilibrium Molecular Dynamics	18
1.3.3 Reverse Non-Equilibrium Molecular Dynamics	19
1.4 Systems of Interest	20
CHAPTER 2: INTERFACIAL THERMAL CONDUCTANCE OF THIOLATE-PROTECTED GOLD NANOSPHERES	21
2.1 Introduction	21
2.2 Interfacial Thermal Conductance of Metallic Nanoparticles	23
2.2.1 Structures of Self-Assembled Monolayers on Nanoparticles	24
2.3 Computational Details	25
2.3.1 Creating a thermal flux between particles and solvent	25
2.3.2 Interfacial Thermal Conductance	27
2.3.3 Force Fields	28
2.3.4 Simulation Protocol	31
2.4 Results	36
2.4.1 Corrugation of the Particle Surface	38
2.4.2 Orientation of Ligand Chains	41
2.4.3 Orientation of Interfacial Solvent	43
2.4.4 Solvent Penetration of Ligand Layer	45
2.4.5 Ligand-mediated Vibrational Overlap	50
2.5 Discussion	51

CHAPTER 3: THERMAL TRANSPORT IS INFLUENCE By NANOPARTICLE SHAPE	54
3.1 Abstract	54
3.2 Introduction	54
3.2.1 Size- and temperature-dependent particle morphologies	56
3.2.2 Theory	57
3.3 Computational Details	59
3.3.1 System Composition	59
3.3.2 Force Fields	61
3.3.3 Simulation Protocol	61
3.4 Results and Discussion	65
3.4.1 Hexane Density	67
3.4.2 Surface Atom Undercoordination	67
3.4.3 Phonon Spectra	74
3.4.4 A Brief Aside	76
3.4.5 A Simple Model for Bare Nanoparticle Conductance	81
3.5 Conclusions	85
BIBLIOGRAPHY	86

FIGURES

1.1	Here an incoming phonon in material A is approaching the interface of materials A and B. The wave has a polarization (p) and frequency (ω) and approaches the interface at an angle (θ) relative to the normal of the interface. The phonon, under the DMM, has two options at the interface: scatter through to material B or scatter back through material A. The probability of transmission is given by τ_{ab} . Due to the fact the DMM must obey detailed balance, the scatter back to material A is $1 - \tau_{ab}$	4
1.2	The initial positions, r , and velocities, v , are established in a system and from the potential energy, forces on the atoms is found. From the forces, positions can be changed then the velocities can be updated. The time can be moved forward and the process repeated at the calculated forces step until the desired time is reached.	8
1.3	This figure is an example of periodic boundaries in two dimensions. Here the middle most cell (colored square) is the system created and each surrounding cell is an 'image' of the original. As can be seen in the relation between particle A and C, sometimes the image particle is the closer interaction and would be within the cutoff when calculating interactions.	12
1.4	This is a visualization of a gold particle solvated in water within the Langevin Hull taken from Vardeman <i>et. al.</i> [1]. The temperature and pressure bath interact with only the outer most atoms on the hull, the grey translucent surface. At each time step the hull is computed to ensure the atoms are interacting in the as edge atoms or as interior atoms.	14
2.1	Topologies of the thiolate capping agents and solvent utilized in the simulations. The chemically-distinct sites (S, CH ₂ , CH ₃ , CHe, CHa and CH ₂ a) are treated as united atoms. Most parameters are taken from references 2, 3 4. Cross-interactions with the Au atoms were adapted from references 5, 6, and 7.	26

2.2	A 25 Å radius gold nanoparticle protected with a half-monolayer of TraPPE-UA dodecanethiolate (C_{12}) ligands and solvated in TraPPE-UA hexane. The interfacial thermal conductance is computed by applying a kinetic energy flux between the nanoparticle and an outer shell of solvent.	34
2.3	Radial temperature profile for a 25 Å radius particle protected with a 50% coverage of TraPPE-UA butanethiolate (C_4) ligands and solvated in TraPPE-UA hexane. A kinetic energy flux is applied between RNEMD region A and RNEMD region B. The size of the temperature discontinuity at the interface is governed by the interfacial thermal conductance.	35
2.4	Interfacial thermal conductance (G) values for 4 sizes of solvated nanoparticles that are bare or protected with a 50% coverage of C_4 , C_8 , or C_{12} thiolate ligands. Ligands of different flexibility are shown in separate panels. The middle panel indicates ligands which have a single carbon-carbon double bond in the penultimate position.	37
2.5	Fraction of gold atoms with fcc ordering as a function of radius for a 10 Å radius nanoparticle. The decreased fraction of fcc-ordered atoms in ligand-protected nanoparticles relative to bare particles indicates restructuring of the nanoparticle surface by the thiolate sulfur atoms.	40
2.6	Computed corrugation values for 4 sizes of solvated nanoparticles that are bare or protected with a 50% coverage of C_4 , C_8 , or C_{12} thiolate ligands. The smallest (10 Å) particles show significant disruption to their crystal structures, and the length and stiffness of the ligands is a contributing factor to the surface disruption.	42
2.7	The two extreme cases of ligand orientation relative to the nanoparticle surface: the ligand completely outstretched ($\cos(\theta) = -1$) and the ligand fully lying down on the particle surface ($\cos(\theta) = 0$).	44
2.8	Computed ligand and interfacial solvent orientational P_2 values for 4 sizes of solvated nanoparticles that are bare or protected with a 50% coverage of C_4 , C_8 , or C_{12} alkanethiolate ligands. Increasing stiffness of the ligand orients these molecules normal to the particle surface, while the length of the ligand chains works to prevent solvent from lying flat on the surface.	46
2.9	Radial density profiles for 25 Å radius nanoparticles with no ligands (circles), C_4 ligands (squares), C_8 ligands (diamonds), and C_{12} ligands (triangles). Ligand density is indicated with filled symbols, solvent (hexane) density is indicated with open symbols. As ligand chain length increases, the nearby solvent is excluded from the ligand layer. The conjugated ligands (upper panel) can create a separated solvent shell within the ligand layer and also allow significantly more solvent to penetrate close to the particle.	48

2.10 Density overlap parameters (O_{l-s}) for solvated nanoparticles protected by thiolate ligands. In general, the rigidity of the fully-conjugated ligands provides the easiest route for solvent to enter the interfacial region. Additionally, shorter chains allow a greater degree of solvent penetration of the ligand layer.	49
2.11 The low frequency portion of the vibrational density of states for three chemical components (gold nanoparticles, C ₁₂ ligands, and hexane solvent). These densities of states were computed using the velocity autocorrelation functions for atoms in the interfacial region, constructed with velocities projected onto a direction normal to the interface.	52
3.1 Interfacial thermal conductance, G , for bare gold nanospheres, cuboctahedra, and icosahedra in contact with hexane solvent. Conductances for flat Au(111), Au(100), and Au(110) interfaces are indicated with dashed horizontal lines. A fit using the model of Tascini <i>et al.</i> is shown along with the predicted value of $G(\infty)$, the infinite particle limit.	66
3.2 Hexane density as a function of distance from the interfacial gold for the (111), (110), and (100) facets. The solvent in the (111) and (100) systems display nearly identical density profiles. Because the lowest-coordinated gold atoms on the (110) facet have a relatively low surface density, the hexane molecules are able to get closer to these undercoordinated atoms.	68
3.3 Locations of undercoordinated atoms on common gold facets. The dark gold atoms indicate atoms of a particular coordination number, cyan atoms denote the first nearest neighbors of these atoms, and the partially transparent lattice illustrates the location of the atoms in the larger gold structure. (111) surfaces (lower left) display atoms with CN=9, while (100) surfaces (upper left) display atoms with CN=8, and (110) surfaces present surface atoms with CN=7 and buried atoms with CN=11.	71
3.4 The normalized low frequency density of states (DOS) of the surface atoms with the coordination number of 6, 7, 8, 9 and 11, corresponding to the vertices of the icosahedra, Au(110), Au(100), Au(111) and sub-surface Au(110), respectively. Note that CN=11 atoms near a surface are found adjacent to atoms with lower coordination (e.g. CN=7), so the high frequency peak at 138 cm ⁻¹ is present for both CN=11 and CN=7. Low frequency contributions at ~ 70 cm ⁻¹ are enhanced for surface atoms with CN=7, 8, and 9.	73

3.5 The coordination number of surface atoms as a function of particle size. Filled data points are sampled from simulations, while the dashed lines correspond to ideal icosahedral and cuboctahedral solids. In the spherical case, the large radius limits are shown with open symbols. The large radius limit for the spheres approaches a constant density for all undercoordinated sites, while for the icosahedra, the 9-coordinated (111) facet dominates. In larger cuboctahedra, the relative fraction of 8- and 9-coordinated surface atoms is largely independent of particle size.	75
3.6 The fraction of FCC-like local environments as a function of radius from the center of 40 Å nanoparticles. The spheres and cuboctahedra are originally cut from a FCC lattice, so the local ordering persists even close to the surface. Icosahedra are constructed as shells surrounding a perfectly icosahedral central core of 13 atoms. Non-FCC ordering persists throughout these simulations.	78
3.7 The projected vibrational density of states (Eq. 3.4) for individual layers in the largest gold nanoparticles (top: spheres, middle: icosahedra, bottom: cuboctahedra). In all systems, the surface layer (green) is significantly enhanced at low frequencies and is shifted down by $\sim 20 \text{ cm}^{-1}$. The Au (bulk) curve shown for comparison is from a perfect FCC lattice in periodic boundary conditions.	79
3.8 The projected vibrational density of states for all gold atoms (top panel) shows that the phonons in FCC-like nanoparticles (spheres, cuboctahedra) have similar frequency representation, while the non-FCC structures (icosahedra) have significantly altered “bulk” spectra. For surface atoms (bottom panel), the differences in surface undercoordination appear at higher frequencies. These spectra were computed for the largest particles in each of the different morphologies.	80
3.9 The normalized low frequency density of states (DOS) of the interfacial solvent and the gold particle for the icosahedral and spherical systems.	82
3.10 Structurally-predicted thermal conductance values from Eq. (3.18) compared with the simulated thermal conductance values. Error bars indicate the standard error computed using five replica simulations.	84

TABLES

1.1	Constitutive and balance equations related to the transport coefficients of diffusivity, D , thermal conductivity, λ , and shear viscosity, η	15
2.1	Non-bonded interaction parameters (including cross interactions with Au atoms).	29
2.2	Bond parameters.	30
2.3	Bend angle parameters. The central atom in the bend is atom j	32
2.4	Torsion parameters. The central atoms for each torsion are atoms j and k , and wildcard atom types are denoted by “X”. All c_n parameters have units of kcal/mol. The torsions around carbon-carbon double bonds are harmonic and assume a trans (180°) geometry. The force constant for this torsion is given in kcal mol $^{-1}$ degrees $^{-2}$	33
3.1	Composition of the solvated planar facet systems and the physical extent of the gold slabs (L_x , L_y , and L_z). The hexane molecules occupy the remainder of a 100 Å box (length measured along the z -axis).	60
3.2	Composition of the solvated nanosphere simulations.	60
3.3	Composition of the solvated icosahedral nanoparticle simulations.	62
3.4	Composition of the solvated cuboctahedral nanoparticle simulations.	63
3.5	Surface densities (Å $^{-2}$) of undercoordinated atoms in ideal geometries. ℓ (Å) is the lattice constant of the underlying FCC lattice. The spheres and cuboctahedra are calculated using a gold FCC lattice with $\ell = 4.08$ Å. For cuboctahedral particles, the radius (r) is computed using Eq. (3.15).	69
3.6	The density of undercoordinated gold atoms at the surface of a facet.	74
3.7	Parameters of the Model in Eq. (3.18).	83

CHAPTER 1

INTRODUCTION

This introductory chapter explores the basics of heat transfer and molecular dynamics. The challenges existing in the current thermal transport methods and methods of finding transport quantities using molecular dynamics are included. Finally, systems of interest are presented for the application of thermal transport using molecular dynamics. The remaining chapters go on to use the methods described here to examine systems of interest in a chronological order.

The first system, gold nanospheres of varying size and ligand, is presented in Chapter 2. The system looks at three different variables to characterize the systems: particle size, ligand length, and ligand rigidity. Through looking at the vibrational density of states and the density profiles for the systems, two important factors for heat transport can be determined: the vibrational overlap of the material at the interface and the physical proximity/overlap of the material at the interface. This information gives relevant particle design for the ligand aspect of the system, while no clear trend for particle radius could be established.

Chapter 3 takes a closer look at the particle surface and size dependence. In this work the particles are left bare and range in size over three different geometries: sphere, icosahedron, and cuboctahedron. This was done in an attempt to detangle the size dependence and the ligand dependence of the previous study. The three different morphologies give distinct vibrational freedoms at the particle surface, allowing for different thermal conductivity. In addition to the particle systems, planar systems displaying the prominent facets of the particles were studied. This work strengthens

the need for a proximity factor of thermal transport suggested in the previous studies through the result that not only the vibrational freedom of the material at the interface matters, but the amount of the material that is transferring heat is essential to consider. This is most clearly seen through the coordination population of the surface atoms in the planar systems.

Chapter 4 presents a combination of the concepts in the previous chapters through the study of small nanoparticles both in isolation and in an array. The $Au_{144}PET_{60}$ are approximately 5 Å in radius and have a crystal structure found at very low temperatures which is an appropriate starting structure for our simulations. A unique aspect of these particles, and similar small structures, is that the ligand layer has gold atoms pulled out of the surface. This leads to low coordination of the outer most gold atoms, that now exhibit a different vibrational spectrum and thermal conductivity. These particles were simulated in two different solvents to look at solvent effects of the thermal conductivity of these particles.

Finally, Chapter 5 looks forward to potential applications of a new fluctuating charge embedded method to be applied to metal surfaces and particles in polarizable solvents. This new method would allow for the examination of charge effects on thermal transport and arrangement of solvent at the surface of the metal.

1.1 Heat Transport

The classical definition of temperature is a quantity that describes a thermal equilibration phenomena. At the macroscopic level, heat can be transferred in three ways: conduction, convection, and radiation.⁸ In equipartition theorem, where the average kinetic energy of a particle is $\frac{3k_B T}{2}$, the temperature is a portion of the kinetic energy of the system.⁹ When the kinetic energy is distributed evenly among all independent parts of the system, the heavy atoms in a system would have an average velocity slower than the lighter atoms in the system at the same temperature.

On the microscopic level, heat moves through different paths depending on the composition of the system.⁸ In a gas, heat is transferred primarily through collisions, while in semi-conductors thermal energy moves through the propagation of vibrations in the solid, a phonon. A phonon is a quantized lattice wave that traverses the material with a longitudinal or transverse polarization.¹⁰ In systems, like metals, where the material has a solid lattice and a sea of electrons, both phonons and electron heat transfer should be considered.¹⁰ Electrons in a metal system are typically treated as an electron gas. Electrons travel at velocities that are approximately three orders of magnitude larger than phonons, therefore the electron contribution dominates heat transfer in metals and is important when considering bulk thermal conductance of metals. At a metal/non-metal interface the thermal conductance through the non-metal is dominated by phonons, rather than electronic contributions.^{8, 11, 12}

1.1.1 Heat Transfer at Interfaces

Further examination of phonons as the only heat carriers can be done at the interface of two materials. If the phonon is traveling through material A and approaches material B with frequency ν , with angles ϕ and θ normal to the interface; there is a transmission probability, $\tau_{a \rightarrow b}(\omega)$, that the wave will continue into material B (see Figure 1.1).¹³ The transmission probability must satisfy detailed balance. There are two major models that have predictions for behavior of heat transfer at the interface: acoustic mismatch model (AMM) and diffuse mismatch model (DMM).¹³

1.1.2 Acoustic Mismatch Model

In the acoustic mismatch model the transmission probability- the total fraction of energy transmitted across the interface- is dependent on the acoustic impedance of the material, Z_i . The AMM evaluates the transmission coefficient through a continuum approach.¹⁴ This model uses the acoustic transmission and reflection between the two

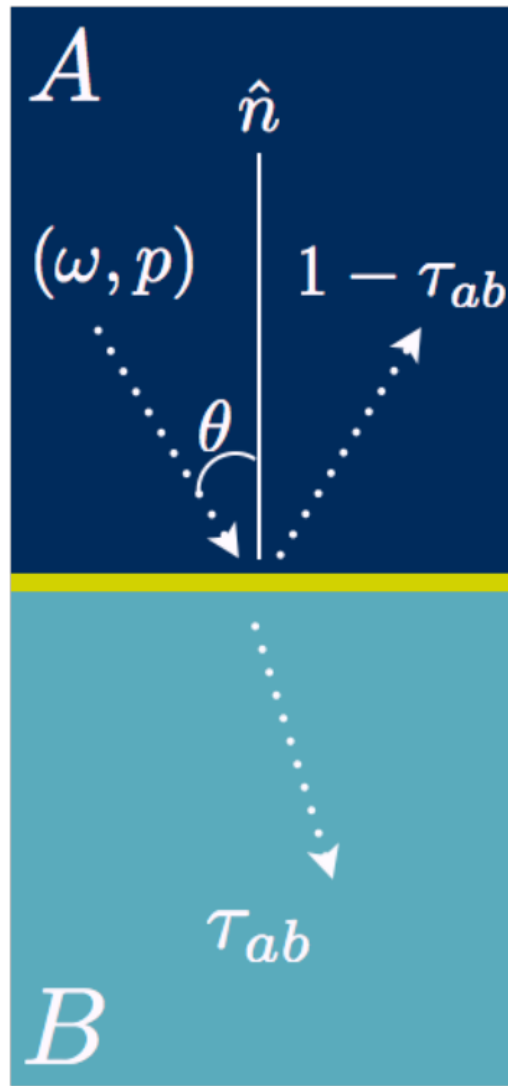


Figure 1.1. Here an incoming phonon in material A is approaching the interface of materials A and B. The wave has a polarization (p) and frequency (ω) and approaches the interface at an angle (θ) relative to the normal of the interface. The phonon, under the DMM, has two options at the interface: scatter through to material B or scatter back through material A. The probability of transmission is given by τ_{ab} . Due to the fact the DMM must obey detailed balance, the scatter back to material A is $1 - \tau_{ab}$.

materials and ignores the granularity of the materials. Therefore the AMM would be most appropriate for low temperatures where the thermal spectrum is dominated by long wavelength phonons.¹⁵

Each phonon can be transmitted in three ways; one longitudinal and two transverse. Likewise the phonon can be reflected in the same fashion, giving six different paths for a sound wave to interact with the interface. This problem is usually simplified by using the acoustic analog of Snells law:

$$\tau_{ab}(\theta, p) = \frac{4 \frac{p_2 \nu_{p,2}}{p_1 \nu_{p,1}} \cos \theta_{p,2}}{\left(\frac{p_2 \nu_{p,2}}{p_1 \nu_{p,1}} + \frac{\cos \theta_{p,2}}{\cos \theta_{p,1}} \right)^2} \quad (1.1)$$

where θ are related to the analog of Snell's law through the frequency: $\frac{\sin \theta_1}{\nu_1} = \frac{\sin \theta_2}{\nu_2}$.

Transmission can be simplified through using acoustic impedances:

$$\tau_{ab}(\theta, p) = \frac{4 Z_a Z_b}{(Z_a + Z_b)^2} \quad (1.2)$$

where Z is the acoustic impedance of each material, $Z_a = \rho_a v_a$. Within the acoustic impedance, ρ is density of states and v is the speed of sound in the material.

More complex treatments of the sound waves¹⁶ and treatments accounting for the interfacial bonding¹⁷ through the AMM have been studied. These modifications result in values that are lower than traditional AMM, therefore much below the experimental measurements of the systems.^{12, 18}

1.1.3 Diffuse Mismatch Model

The diffuse mismatch model assumes that the phonon has two options when the wave meets the interface: the phonon can transfer into material B or is reflected back into material A (see Figure 1.1). It operates under the assumption that all phonons at the interface are scattered randomly; meaning that all memory of the direction

and polarization are lost. The phonon only keeps the frequency constant during the interaction of the two materials. Hence all probability of the phonon to propagate into a material is dependent of the material's density of states.

Under the DMM, the thermal conductance at an interface between a and b can be approximated,

$$G_{ab} = \frac{1}{4\pi} \sum_p \int_{\omega} \int_{\theta} \int_{\phi} \hbar\omega \frac{\partial f}{\partial T} v_a \rho_a \tau_{ab} \cos \theta \sin \theta d\theta d\phi d\omega \quad (1.3)$$

where f is the Bose-Einstein distribution function, $v_a(\omega, p)$ is the group velocity (on side a) for a phonon characterized by frequency ω , moving in direction (θ, ϕ) with polarization p . The relevant material properties are the density of phonon states, $\rho_a(\omega, p)$, and the transmission probability, $\tau_{ab}(\omega, p)$, at the interface.^{13, 19, 20} The DMM also assumes that phonons scatter into states with the same frequency on either side, and that the scattering phonons lose memory of their incident angles. This requires a symmetry in the transmission probabilities,

$$\tau_{ab}(\omega) = 1 - \tau_{ba}(\omega) \quad (1.4)$$

The DMM has a number of significant issues, particularly when the Debye model does a poor job representing the density of states, or where there is a fictitious boundary between identical materials (where the DMM predicts a non-zero resistance).¹³ There is also an assumption of detailed balance built-in to the model,⁸ which requires the two sides to be at equilibrium. The DMM is more appropriate for modeling thermal transport at noncryogenic temperatures and at rough interfaces because the majority of acoustic phonons at ≥ 300 K have short wavelengths. The wavelengths at these temperatures are comparable to the interatomic spacing in the system.

While attempts to account for interfacial bonding have been made in the AMM, the DMM interfacial methods have not been developed. The interaction of the ma-

terials at the interface has been found to be of significant importance to thermal conductivity^{21–23}, but a factor to include this interaction has yet to be incorporated in the theory. Despite the DMM’s pitfalls, it has been the most commonly used model for the past 30 years.^{11, 12, 18, 24}

1.2 Molecular Dynamics

Molecular dynamics are computer simulations used to study structure and dynamics of atoms and molecules using classical mechanics. A simple algorithm of a molecular dynamics simulation can be described given atoms with initial positions and velocities, forces (using interactions described later) can be calculated that are used to move the atoms, then the time is moved forward and the cycle repeats from calculating the forces (see Figure 1.2). The forces calculated follow from Newton’s equations of motion. The positions and velocities at each time step create a trajectory of the system that is time reversible.

Forces between each pair of atomic sites are computed by an interaction potential, where the forces are the gradient of the scalar potential:

$$\vec{F}(\vec{R}, t) = -\vec{\nabla} \cdot V(\vec{R}) \quad (1.5)$$

These potentials are approximated using intra and inter molecular forces in the system to make an approximate potential energy surface with respect to the nuclear coordinates of the system.²⁵

$$V(\vec{R}) = V_{bonded} + V_{electrostatic} + V_{vdW} + V_{constraints} + V_{hb} \quad (1.6)$$

The simplest of these to start with is the intra-molecular forces V_{bonded} , composed of bonds, bends, torsions. Typical bonding potentials take the form of either harmonic

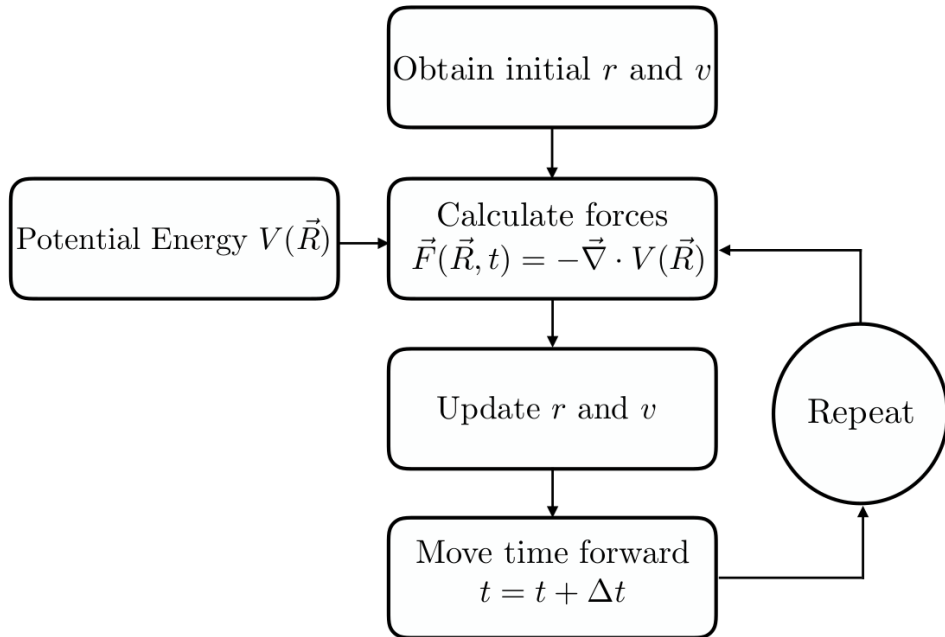


Figure 1.2. The initial positions, r , and velocities, v , are established in a system and from the potential energy, forces on the atoms is found. From the forces, positions can be changed then the velocities can be updated. The time can be moved forward and the process repeated at the calculated forces step until the desired time is reached.

bonds,

$$V_{bond}(r) = \frac{k_{ij}}{2} (r - r_{ij}^0)^2 \quad (1.7)$$

or Morse bonds,

$$V_{bond}(r) = D_{ij} [1 - \exp^{-\beta(r - r_{ij}^0)}]^2. \quad (1.8)$$

While other potential forms such as cubic and quartic can be used, the main form used in the following work will follow the harmonic form. In the harmonic form there are two variables that need to be provided: k_{ij} and r_{ij}^0 . The former is the spring constant associated with how the bond behaves when stretched and contracted. The latter is the equilibrium bond distance between the two beads.

Similar to the bonding potentials, the bending potentials may take many forms. In this work the harmonic potential,

$$V_{bend}(\theta) = \frac{k_{ijk}}{2} (\theta - \theta_{ijk}^0)^2, \quad (1.9)$$

was used, where θ is the angle between three connecting beads i , j , and k . θ_{ijk}^0 is the equilibrium bend angle and k_{ijk} is the spring constant for the bend.

The potential due to torsions within a bonded system is from the rotation of the plane made from the i , j , and k points relative to the l point:

$$V_{torsions}(\phi_{ijkl}) = c_1[1 + \cos \phi_{ijkl}] + c_2[1 + \cos 2\phi_{ijkl}] + c_3[1 + \cos 3\phi_{ijkl}] \quad (1.10)$$

where the angle ϕ_{ijkl} is $(\hat{r}_{ij} \times \hat{r}_{jk}) \cdot (\hat{r}_{jk} \times \hat{r}_{kl})$ and \hat{r}_{ab} is the unit vector between a and b .

Inter-molecular, or non-bonded interactions, are interactions between molecules which include the electrostatic interactions and van der Waals interactions. The

potential for electrostatic interactions

$$V_{electrostatic} = \frac{q_i q_j}{4\pi\epsilon_0 |r_{ij}|}, \quad (1.11)$$

describes the potential between two charged sites interacting via Coulomb's law. Van der Waals interactions in this work are described via the Lennard Jones potential,

$$V_{vdW} = 4\epsilon \left[\left(\frac{\sigma}{|r_{ij}|} \right)^{12} + \left(\frac{\sigma}{|r_{ij}|} \right)^6 \right] \quad (1.12)$$

where ϵ is the well depth when the distance between the two bodies is the at minimum and σ is the distance the well starts from zero. The $\frac{1}{r^6}$ term is similar to dispersion and the $\frac{1}{r^{12}}$ term is empirically added to have a repulsion term.

The last two terms in the full potential equation, $V_{constraints}$ and V_{hb} , hydrogen bonding, are not relevant and thus will not be discussed in this work.

1.2.1 Representations of Atoms

Within molecular dynamics, which is a lower accuracy method than first principles methods, there are different levels of simplification of the treatment of molecules.²⁵ Chiefly, there are three ways of treating the molecules in a given system that will be discussed here. The first, all-atom, is representing each atom within the system as a bead. Within a molecule these beads share bonds with atoms it is covalently bonded with and experiences bends and torsions within the larger molecule.

The next is a simplified version of the all-atom representation, united-atom, which compresses the hydrogen atoms onto the larger atom to which they were bonded. The mass and atomic radius of this bead is increased according to the amount of hydrogens added.

United-atom calculations are faster due to the decrease in N, the number of atoms. They also are a better representation of heat transport. The vibrations

of the molecules are of paramount importance in thermal transport and bonds to hydrogen have a very quick vibration. In molecular dynamics the vibrational modes are occupied equally due to equipartition of the energy, thus the vibrational spectrum of the molecule will have high frequency hydrogen peaks. These high frequencies are irrelevant in thermal transport and thus all-atom simulations add expenses and information that detracts from the low frequency picture of the system.

The last treatment discussed here is coarse-grain systems. These systems are further simplifications of the system. In coarse-grain systems, beads from the united atom model would be grouped into a single bead that represents a small molecule. The granularity of the beads can be adjusted from system to system and depends on the property desired and the timescale of the simulation. In general, coarse-graining is used more widely for biologically relevant systems (i.e. proteins, lipids, etc.).

1.2.2 Boundary Conditions

In many simulations the desired quantity is a bulk property. To simulate a full bulk system would require too many atoms and too much time than tangibly possible within the lifetime of a person. Not to mention that the large box would have effects from the edges of the box. So how can the surface effects be avoided and simulate a bulk-like simulation?

In periodic boundary conditions the above issues can be addressed. A simulation cell that has bulk-like density can reproduce bulk properties. Periodic boundary conditions are typically applied to orthorobic simulation boxes, though any space filling geometry works. An 'image' copy of the the simulation box is replicated in every direction. For example, in two dimensions periodic boundaries are represented in Figure 1.3, where the simulation box has eight copies. In three dimensions, twenty-six images of the original box surround the simulation cell, for an orthorobic box.

Within the simulation, only the particles in the central box are necessary to track.

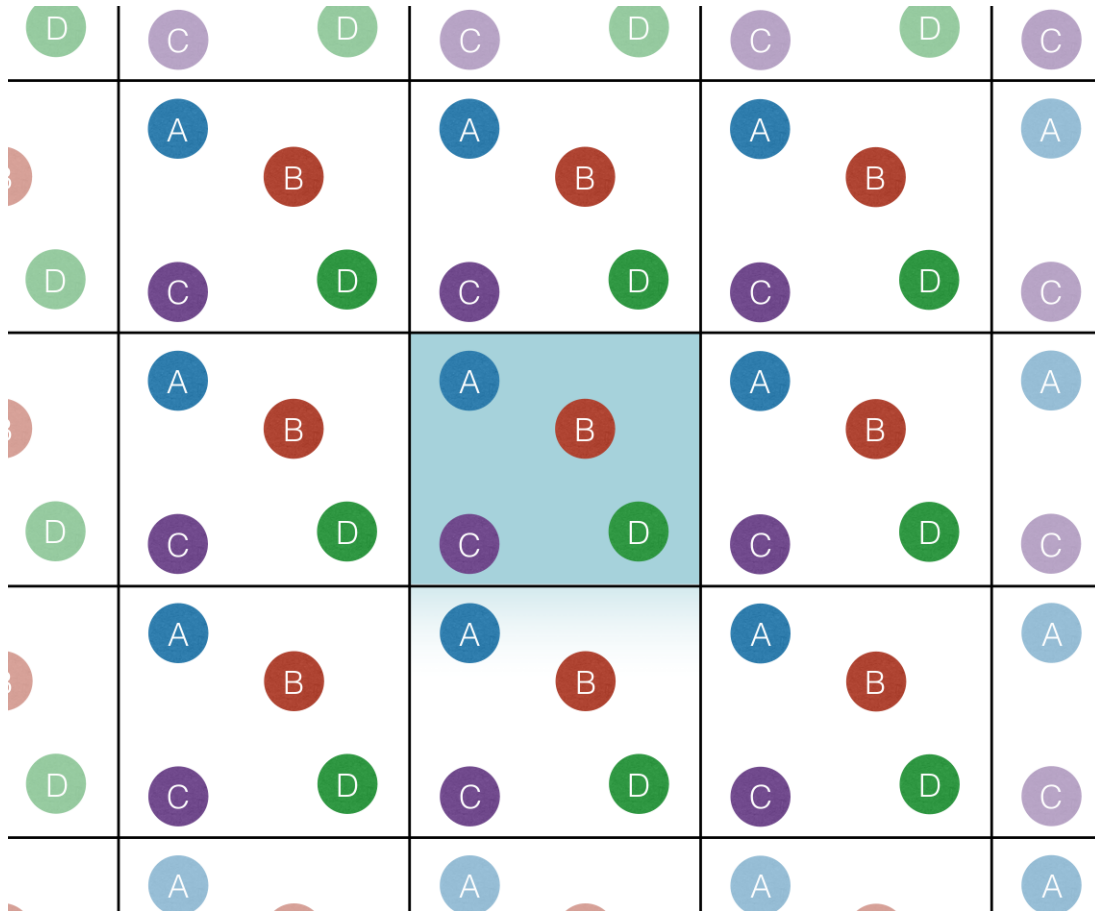


Figure 1.3. This figure is an example of periodic boundaries in two dimensions. Here the middle most cell (colored square) is the system created and each surrounding cell is an 'image' of the original. As can be seen in the relation between particle A and C, sometimes the image particle is the closer interaction and would be within the cutoff when calculating interactions.

The particles' images in neighboring cells are increments of the box dimension along each principal axis. So if the particle exits the right boundary of the cell, it will return in the box on the left boundary (from the neighboring simulation cell), which preserves the number density of the cell. In addition to periodic boundaries, the minimum image convention is used to make the simulation computationally possible. The minimum image convention is that a given particle only interacts with the closest periodic image of the particle in the system. Along with this idea is a spherical cutoff, where a particle's non-bonded interactions with other particles end at a finite distance, r , from the particle which is less than half the length of periodic box. This ensures that the particle sees one image of each particle and is not interacting with an image of itself.

Though periodic boundaries allows for bulk properties to be found, it creates artificial periodicity in the system and might require an unreasonable system size due to the box structure. Later in this work, simulations of isolated particles are utilized to get single particle properties. These isolated systems implement the Langevin Hull method. While there are several non-periodic methods that allow for a constant pressure, Langevin Hull can handle heterogeneous mixtures of materials with different compressibilities.¹ This method is a modified version of Kohanoff, Caro, and Finnis' method for constant pressure and temperature non-periodic simulations based on Langevin dynamics.^{26, 27}

In the Langevin Hull method the boundary of the system is a completely convex hull made from facets from points triangulated with the outer most atoms of the system. This hull interacts with a system bath that applies constant pressure and provides a thermal bath for the system through the facets of the hull. When looking at thermal properties of a system, the thermal coupling can be turned off to prevent artificial behavior due to the bath.

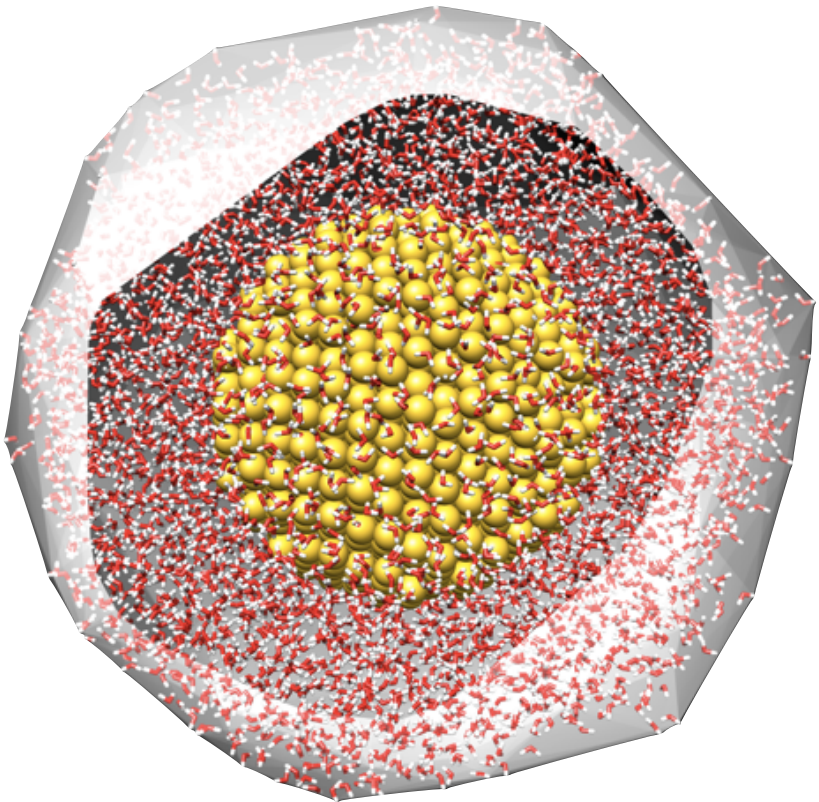


Figure 1.4. This is a visualization of a gold particle solvated in water within the Langevin Hull taken from Vardeman *et. al.*.¹ The temperature and pressure bath interact with only the outer most atoms on the hull, the grey translucent surface. At each time step the hull is computed to ensure the atoms are interacting in the as edge atoms or as interior atoms.

1.3 Transport Coefficients

Transport phenomena are controlled by the constitutive equations that describe how a material responds to various stimuli via transport. The processes that are at the center of transport phenomena concern the transfer of mass, heat, or momentum. The transport of any of those listed would create a measurable flux in the system. The conservation equations conserve the desired property of interest in the presence of a flux. The constitutive equations relate a transport property (diffusion, thermal conductivity, viscosity) to a flux via an empirical relationship. The flux, in all these cases, is proportional to the gradient and a constant of proportionality.

TABLE 1.1

Constitutive and balance equations related to the transport coefficients of diffusivity, D , thermal conductivity, λ , and shear viscosity, η .

Transport coefficients	Constitutive equations	Balance equations
D	$\vec{j} = -D \cdot \vec{\nabla} c(\vec{r}, t)$	$\frac{\partial c(\vec{r}, t)}{\partial t} + \vec{\nabla} \cdot \vec{j} = 0$
λ	$\vec{q} = -\lambda \cdot \vec{\nabla} T(\vec{r}, t)$	$C_p \frac{\partial T(\vec{r}, t)}{\partial t} + \vec{\nabla} \cdot \vec{q} = 0$
η	$\sigma_{x,z} = -\eta \cdot \vec{\nabla}_z (\rho v_x)$	$\rho \frac{D\vec{v}(\vec{r}, t)}{Dt} + \vec{\nabla} \cdot \vec{\sigma} = 0$

- Diffusion (Ficks Law): $\vec{j} = -D \cdot \vec{\nabla} c(\vec{r}, t)$

The diffusivity, D , or the diffusion coefficient is the proportionality between the concentration gradient of a species and the mass flux, j .

- Thermal Conductivity (Fouriers Law): $\vec{q} = -\lambda \cdot \vec{\nabla}T(\vec{r}, t)$

The local heat flux density, q , is equal to the conductivity of the material, λ , and the temperature gradient through the material. Therefore, λ indicates the material's ability to conduct heat due to a temperature gradient.

- Viscosity (Newtons Law of Viscosity): $\sigma_{x,z} = -\eta \cdot \vec{\nabla}_z(\rho v_x)$

The shear stress in the fluid, σ , is equal to the shear viscosity, η , and the velocity gradient, $\vec{\nabla}_z(\rho v_x)$.

All the transport coefficients (D , λ , η) describe how an instantaneous flux in a system relates to a corresponding gradient. Table 1.1 lists how the transport coefficients are involved in constitutive equations, where ρ is the density and C is the heat capacity of a material.

Transport phenomena are utilized in many fields, such as chemistry, physics, chemical engineering, electrical engineering, mechanical engineering, to obtain the transport coefficients to optimize a system. Atomistic simulations can provide insight for tuning experimental design. The three main ways to calculate transport coefficients, with a focus on thermal conductivity, will be discussed in detail in the following sections.

1.3.1 Equilibrium Molecular Dynamics

Transport properties from classical molecular dynamics simulations can be found through many methods. Equilibrium Molecular Dynamics (EMD) simulations use the most straight forward method. Using a relevant time correlation function to the transport coefficient of interest, under linear response theory, the transport coefficient can often be found.^{28–33} In most cases either the Einstein relation or the Green-Kubo formulation are utilized in EMD.

The Einstein relation for thermal conductivity uses the Helfand moment, $G^\lambda(t)$,

which is a centroid of the energies:

$$G^\lambda(t) = \sum_{a=1}^N r_a(E_a - \langle E_a \rangle) \quad (1.13)$$

where E is the energies of the particles. Energy is given by the following:

$$E_a = \frac{p_a^2}{2m} + \frac{1}{2} \sum_{b \neq a} U(r_{ab}) \quad (1.14)$$

where p is the momentum, m is the mass, and $U(r_{ab})$ is the potential energy.

The Einstein relation can find the thermal conductivity using the fluctuations in the Helfand moment:

$$\lambda = \lim_{N,V,t \rightarrow \infty} \frac{1}{2k_B T^2 V t} \left\langle \left[G^\lambda(t) - G^\lambda(0) \right]^2 \right\rangle \quad (1.15)$$

where k_B is the Boltzmann constant, T is the temperature, V is the volume, and t is the time.

The equivalent Green-Kubo relation for thermal conductance is

$$\lambda = \frac{1}{3V k_B T^2} \int_0^\infty dt \langle q(t) \cdot q(0) \rangle \quad (1.16)$$

where q is the heat current. The heat current can be found through

$$q(t) = \sum_{i=1}^N E_i \vec{v}_i + \frac{1}{2} \sum_{j \neq i} \vec{r}_{ij} (f_{ij} \cdot \vec{v}_j). \quad (1.17)$$

The first term is a summation of the energy times the velocity of all particles. The second term contains the force on atom i due to atom j , f_{ij} . In contrast to the Einstein relation where the mass, velocity, and potential are easily obtained from an equilibrium simulation, the heat current requires a little more effort.

Both the Einstein and Green-Kubo relations for thermal conductivity rely on correlation functions, where the long-time tails are able to significantly contribute to the integrate area and need long simulation times to achieve convergence. The noise and poor convergence in the long-time tails give a poor estimation for the thermal conductivity and thus EMD simulations are not the best method for calculating this transport coefficient. Moreover, these calculations would have further complications when the systems would contain an interface or a non-homogeneous.

1.3.2 Non-Equilibrium Molecular Dynamics

Since EMD has limitations due to the noise in the correlation function, methods in non-equilibrium molecular dynamics, NEMD, were developed that introduces a gradient into the simulations.^{34–37} Typically these methods are used to impose a temperature or velocity gradient on a system to measure the corresponding transport coefficient.^{34–46} With linear response of a flux due to the applied gradient, the transport coefficient can be calculated using the constitutive equation: $J_z = -\lambda \frac{\partial T}{\partial z}$, where $\frac{\partial T}{\partial z}$ is the imposed piece and J_z is the measured flux. In NEMD, the temperature gradient is imposed by choosing sections of the simulation box to have particular temperatures. For example, a center portion of the system will be set to high temperature and the edges set to a lower temperature to impose the gradient. The imposed thermal gradient must be relatively small to maintain a linear relationship between the flux and the gradient. The corresponding transport coefficient, thermal conductivity, can be found if the linear response holds.

Accurately measuring the thermal flux from the imposed gradient is difficult. This method requires thermostats to maintain the thermal gradient which means that it does not ensure momentum or energy conservation and that simulations are restricted to the canonical ensemble. Additionally, in heterogeneous systems, particularly with interfaces, it can be difficult to know what the shape of the imposed gradient should

be at the boundary of materials.

1.3.3 Reverse Non-Equilibrium Molecular Dynamics

Reverse non-equilibrium molecular dynamics (RNEMD) methods impose an unphysical flux and measure the gradient that develops.^{47–49} Imposed flux methods are preferable because the simulation imposes the difficult to measure quantity, the flux, causing the system to develop a gradient, which is easier to measure, between the regions where the flux is imposed. Since the measurement of a gradient is less complex, the imposed flux methods will typically take less time to obtain converged results, therefore the simulations are less time intensive and less costly.

The original RNEMD formulation imposes an artificial momentum flux between parallel slabs of material separated in the simulation cell. The flux was created by periodically swapping the momentum between molecules in each of the slabs in a homogeneous system.⁴⁷ This method was modified to obtain other transport coefficients⁴⁸ and to handle heterogeneous systems.⁵⁰ An attractive feature of RNEMD is that the algorithm conserves total linear momentum and total energy. However, issues with large fluxes can result in non-linear gradients, where linear response can not be used to find the transport coefficient.⁵¹

This method has become widely used for thermal and mechanical properties of homogeneous and heterogeneous systems of solids and liquids^{47, 48, 51}, as well as, interfaces.^{52–55} Gradients near interfaces exhibit distinct behavior at the boundaries of dissimilar materials.

Recent advances in RNEMD methodology have involved scaling particle velocities instead of swapping. The scaling method uses constraint equations that require the simulation to conserve total energy and total linear momentum.^{49, 54} In addition, this RNEMD method has been extended to handle non-periodic heterogeneous systems.⁵⁶

1.4 Systems of Interest

The systems that are explored in this work contain a gold substrate or particle in solvent with heat transport from the gold to the solvent. Thermal properties of gold particles have been of great experimental interest, particularly detangling the important factors for transport: particle size,^{57–61} composition,^{62, 63} surface modification,^{58, 60, 63–68} surface supports,⁶⁹ exposed surface facets,⁶⁶ and the chemical details of the environment.^{59, 63, 65, 67, 69, 70}

Three distinct studies examining interfacial thermal conductivity and heat transport will be explored with three different systems in this work. The first system has nanospheres with a range of particle radii and a ligands with different length and rigidity.⁶⁰ The second system strips away the ligand layer and looks at bare particles with the intention of finding the difference in particle morphology.⁷¹ How exactly does the surface of the particle matter in heat transport? The third system looks at a more complex problem: how does the particle size and the system solvent change thermal conductivity of a nanoarray? To simplify the atomistic models, we use a united-atom model for the ligand layer and solvent. All the particle systems use Langevin Hull¹ and RNEMD methods for non-periodic systems.⁵⁶

CHAPTER 2

INTERFACIAL THERMAL CONDUCTANCE OF THIOLATE-PROTECTED GOLD NANOSPHERES

2.1 Introduction

Molecular dynamics simulations of thiolate-protected and solvated gold nanoparticles were carried out in the presence of a non-equilibrium heat flux between the solvent and the core of the particle. The interfacial thermal conductance (G) was computed for these interfaces, and the behavior of the thermal conductance was studied as a function of particle size, ligand flexibility, and ligand chain length. In all cases, thermal conductance of the ligand-protected particles was higher than the bare metal–solvent interface. A number of mechanisms for the enhanced conductance were investigated, including thiolate-driven corrugation of the metal surface, solvent ordering at the interface, solvent-ligand interpenetration, and ligand ordering relative to the particle surface. Only the smallest particles exhibited significant corrugation. All ligands permitted substantial solvent-ligand interpenetration, and ligand chain length has a significant influence on the orientational ordering of interfacial solvent. Solvent – ligand vibrational overlap, particularly in the low frequency range ($< 80\text{cm}^{-1}$) was significantly altered by ligand rigidity, and had direct influence on the interfacial thermal conductance.

Heat transport across various nanostructured interfaces has been the subject of intense experimental interest,^{53, 62, 72–77} and the interfacial thermal conductance, G , is the principal quantity of interest for understanding interfacial heat transport.⁷⁸

Because nanoparticles have a significant fraction of their atoms at the particle / solvent interface, the chemical details of these interfaces govern the thermal transport properties. Time-domain thermoreflectance (TDTR) measurements on planar self-assembled monolayer (SAM) junctions between quartz and gold films showed that surface chemistry, particularly the density of covalent bonds to the gold surface, can control energy transport between the two solids.⁷⁹ Experiments and simulations on three-dimensional nanocrystal arrays have similarly shown that surface-attached ligands mediate the thermal transport in these materials, placing particular importance on the overlap between the ligand and nanoparticle vibrational densities of states.^{63, 65} Likewise, simulations of polymer-coated gold nanoparticles in water have shown that the surface coating introduces a dominant thermal transport channel to the surrounding solvent.⁸⁰

For ligand-protected nanoparticles in a solvent, there may be three distinct heat transfer processes: (1) from the particles to the ligands, (2) vibrational energy transfer along the length of the ligand, followed by (3) heat transport from the ligand to the surrounding solvent.⁸¹

Heat transport at the gold-alkylthiolate-solvent interface has been previously explored both through molecular dynamics simulations and via TDTR.^{54, 55, 82, 83} Most of these studies have found that alkylthiolates enhance the thermal conductance to the solvent, and that the vibrational overlap provided by the chemically-bound ligand species plays a role in this enhancement.

Reverse nonequilibrium molecular dynamics (RNEMD) methods⁴⁷ have been previously applied to calculate the thermal conductance at flat (111) metal / organic solvent interfaces that had been chemically protected by varying coverages of alkanethiolate groups.⁵⁴ These simulations suggested an explanation for the increased thermal conductivity at alkanethiol-capped metal surfaces compared with bare metal interfaces. Specifically, the chemical bond between the metal and the ligand intro-

duces a vibrational overlap that is not present without the protecting group, and the overlap between the vibrational spectra (metal to ligand, ligand to solvent) provides a mechanism for rapid thermal transport across the interface. The simulations also suggested that this phenomenon is a non-monotonic function of the fractional coverage of the surface, as moderate coverages allow energy transfer to solvent molecules that come into close contact with the ligands.

Similarly, simulations of mixed-chain alkylthiolate surfaces showed that solvent trapped close to the interface can be efficient at moving thermal energy away from the surface.⁵⁵ Trapped solvent molecules that were orientationally aligned with nearby ligands were able to increase the thermal conductance of the interface. This indicates that the ligand-to-solvent vibrational energy transfer is a key feature for increasing particle-to-solvent thermal conductance.

RNEMD methods have been extended for use in non-periodic geometries by creating scaling/shearing moves between concentric regions of a simulation.⁵⁶ In this section, a non-periodic variant of RNEMD has been applied to investigate the role that curved nanoparticle surfaces play in heat and mass transport. On planar surfaces, it has been seen that orientational ordering of surface protecting ligands had a large effect on the heat conduction from the metal to the solvent.⁵⁵ Smaller nanoparticles have high surface curvature that creates gaps in well-ordered self-assembled monolayers, and the effect of those gaps on the thermal conductance is unknown.

2.2 Interfacial Thermal Conductance of Metallic Nanoparticles

For a solvated nanoparticle, it is possible to define a critical value for the interfacial thermal conductance,

$$G_c = \frac{3C_s\Lambda_s}{RC_p} \quad (2.1)$$

which depends on the solvent heat capacity, C_s , solvent thermal conductivity, Λ_s , particle radius, R , and nanoparticle heat capacity, C_p .⁶² In the limit of infinite interfacial thermal conductance, $G \gg G_c$, cooling of the nanoparticle is limited by the solvent properties, C_s and Λ_s . In the opposite limit, $G \ll G_c$, the heat dissipation is controlled by the thermal conductance of the particle / fluid interface. It is this regime with which this study is concerned, where properties of ligands and the particle surface may be tuned to manipulate the rate of cooling for solvated nanoparticles. Based on estimates of G from previous simulations as well as experimental results for solvated nanostructures, gold nanoparticles solvated in hexane are in the $G \ll G_c$ regime for radii smaller than 40 nm. The particles included in this study are more than an order of magnitude smaller than this critical radius, therefore the heat dissipation should be controlled entirely by the surface features of the particle / ligand / solvent interface.

2.2.1 Structures of Self-Assembled Monolayers on Nanoparticles

Though the ligand packing on planar surfaces has been characterized for many different ligands and surface facets, it is not obvious *a priori* how the same ligands will behave on the highly curved surfaces of spherical nanoparticles. Thus, as new applications of ligand-stabilized nanostructures have been proposed, the structure and dynamics of ligands on metallic nanoparticles have been studied using molecular simulation,⁸⁴ NMR, XPS, FTIR, calorimetry, and surface microscopies.^{85–89} Badia, *et al.* used transmission electron microscopy to determine that alkanethiol ligands on gold nanoparticles pack approximately 30% more densely than on planar Au(111) surfaces.⁸⁵ Subsequent experiments demonstrated that even at full coverages, surface curvature creates voids between linear ligand chains that can be filled via interdigitation of ligands on neighboring particles.⁸⁶ The molecular dynamics simulations of Henz, *et al.* indicate that at low coverages, the thiolate alkane chains will lie flat

on the nanoparticle surface⁸⁴. Above 90% coverage, the ligands stand upright and recover the rigidity and tilt angle displayed on planar facets. Their simulations also indicate a high degree of mixing between the thiolate sulfur atoms and surface gold atoms at high coverages.

In this work, thiolated gold nanospheres were modeled using a united atom force field and non-equilibrium molecular dynamics. Gold nanoparticles with radii ranging from 10 - 25 Å were created from a bulk fcc lattice. These particles were passivated with a 50% coverage (compared with the coverage densities reported by Badia *et al.*) of a selection of thiolates. Three straight-chain thiolates of varying chain lengths and rigidities were utilized. These are summarized in Figure 2.1. The passivated particles were then solvated in hexane. Details on the united atom force field are given below.

2.3 Computational Details

2.3.1 Creating a thermal flux between particles and solvent

The non-periodic variant of the velocity shearing and scaling RNEMD algorithm (VSS-RNEMD)[56] applies a series of velocity scaling and shearing moves at regular intervals to impose a flux between two concentric spherical regions. The scaling coefficients a and b are solved for to impose a thermal flux between the shells (without an accompanying angular shear).

$$a = \sqrt{1 - \frac{q_r \Delta t}{K_a - K_a^{\text{rot}}}} \quad (2.2)$$

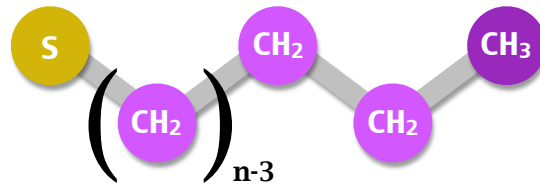
$$b = \sqrt{1 + \frac{q_r \Delta t}{K_b - K_b^{\text{rot}}}} \quad (2.3)$$

at each time interval. These scaling coefficients conserve total kinetic energy and angular momentum subject to an imposed heat rate, q_r . The coefficients also depend on the instantaneous kinetic energy, $K_{\{a,b\}}$, and the total rotational kinetic energy of

Species **Structure**

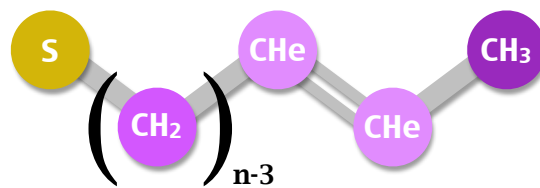
alkanethiolates

$n = 4, 8, 12$



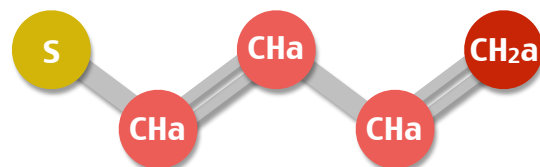
penultimate
alkenethiolates

$n = 4, 8, 12$

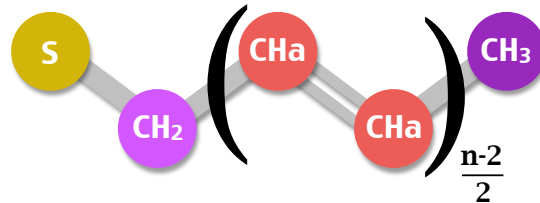


conjugated
alkenethiolates

$n = 4$



$n = 8, 12$



hexane

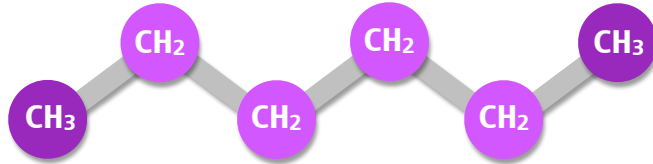


Figure 2.1. Topologies of the thiolate capping agents and solvent utilized in the simulations. The chemically-distinct sites (S, CH₂, CH₃, CHe, CHa and CH₂a) are treated as united atoms. Most parameters are taken from references 2, 3 4. Cross-interactions with the Au atoms were adapted from references 5, 6, and 7.

each shell, $K_{\{a,b\}}^{\text{rot}} = \sum_i m_i (\mathbf{v}_i \times \mathbf{r}_i)^2 / 2$.

The scaling coefficients are determined and the velocity changes are applied at regular intervals,

$$\mathbf{v}_i \leftarrow a (\mathbf{v}_i - \langle \omega_a \rangle \times \mathbf{r}_i) + \langle \omega_a \rangle \times \mathbf{r}_i \quad (2.4)$$

$$\mathbf{v}_j \leftarrow b (\mathbf{v}_j - \langle \omega_b \rangle \times \mathbf{r}_j) + \langle \omega_b \rangle \times \mathbf{r}_j. \quad (2.5)$$

Here $\langle \omega_a \rangle \times \mathbf{r}_i$ is the contribution to the velocity of particle i due to the overall angular velocity of the a shell. In the absence of an angular momentum flux, the angular velocity $\langle \omega_a \rangle$ of the shell is nearly 0 and the resultant particle velocity is a nearly linear scaling of the initial velocity by the coefficient a or b .

Repeated application of this thermal energy exchange yields a radial temperature profile for the solvated nanoparticles that depends linearly on the applied heat rate, q_r . Similar to the behavior in the slab geometries, the temperature profiles have discontinuities at the interfaces between dissimilar materials. The size of the discontinuity depends on the interfacial thermal conductance, which is the primary quantity of interest.

2.3.2 Interfacial Thermal Conductance

The thermal conductance of each spherical shell may be defined as the inverse Kapitza resistance of the shell.[56] To describe the thermal conductance of an interface of considerable thickness – such as the ligand layers shown here – sum the individual thermal resistances of each concentric spherical shell to arrive at the inverse of the total interfacial thermal conductance. In concentric spherical shells, the intermediate temperatures and surface areas remain in the final sum, requiring the use of a series of individual resistance terms:

$$\frac{1}{G} = R_{\text{total}} = \frac{1}{q_r} \sum_i (T_{i+i} - T_i) 4\pi r_i^2. \quad (2.6)$$

The longest ligand considered here is in excess of 15 Å in length, and 10 concentric spherical shells are used to describe the total interfacial thermal conductance of the ligand layer.

2.3.3 Force Fields

Throughout this work, gold – gold interactions are described by the quantum Sutton-Chen (QSC) model.[90] Previous work[54] has demonstrated that the electronic contributions to heat conduction (which are missing from the QSC model) across heterogeneous metal / non-metal interfaces are negligible compared to phonon excitation, which is captured by the classical model. The hexane solvent is described by the TraPPE united atom model,[2] where sites are located at the carbon centers for alkyl groups. The TraPPE-UA model for hexane provides both computational efficiency and reasonable accuracy for bulk thermal conductivity values. Bonding interactions were used for intra-molecular sites closer than 3 bonds. Effective Lennard-Jones potentials were used for non-bonded interactions.

The TraPPE-UA force field includes parameters for thiol molecules[4] as well as unsaturated and aromatic carbon sites.[3] These were used for the thiolate molecules in our simulations, and missing parameters for the ligands were supplemented using fits described below. Bonds are rigid in TraPPE-UA, so although equilibrium bond distances were taken from this force field, flexible bonds were implemented using bond stretching spring constants adapted from the OPLS-AA force field.[91]

Parameters not found in the TraPPE-UA force field for the intramolecular interactions of the conjugated and the penultimate alkenethiolate ligands were calculated

TABLE 2.1

Non-bonded interaction parameters (including cross interactions with Au atoms).

Site	mass (amu)	σ_{ii} (Å)	ϵ_{ii} (kcal/mol)	$\sigma_{\text{Au}-i}$ (Å)	$\epsilon_{\text{Au}-i}$ (kcal/mol)	source
CH ₃	15.04	3.75	0.1947	3.54	0.2146	Refs. 2, 6 and 5
CH ₂	14.03	3.95	0.09141	3.54	0.1749	Refs. 2, 6 and 5
CHene	13.02	3.73	0.09340	3.4625	0.1680	Refs. 3, 6 and 5
S	32.0655	4.45	0.2504	2.40	8.465	Refs. 5 (σ) and 6 (ϵ)
CHar	13.02	3.695	0.1004	3.4625	0.1680	Refs. 3 and 6
CH ₂ ar	14.03	3.695	0.1004	3.4625	0.1680	Refs. 3 and 6

using constrained geometry scans using the B3LYP functional [92, 93] and the 6-31G(d,p) basis set. Structures were scanned starting at the minimum energy gas phase structure for small (C_4) ligands. Only one degree of freedom was constrained for any given scan – all other atoms were allowed to minimize subject to that constraint. The resulting potential energy surfaces were fit to a harmonic potential for the bond stretching,

$$V_{\text{bond}} = \frac{k_{\text{bond}}}{2} (r - r_0)^2, \quad (2.7)$$

and angle bending potentials,

$$V_{\text{bend}} = \frac{k_{\text{bend}}}{2} (\theta - \theta_0)^2. \quad (2.8)$$

TABLE 2.2

Bond parameters.

<i>i</i>	<i>j</i>	<i>r</i> ₀ (Å)	<i>k</i> _{bond} (kcal/mole/Å ²)	source
CH ₃	CH ₃	1.540	536	Refs. 2 and 91
CH ₃	CH ₂	1.540	536	Refs. 2 and 91
CH ₂	CH ₂	1.540	536	Refs. 2 and 91
CHene	CHene	1.330	1098	Refs. 3 and 91
CH ₃	CHene	1.540	634	Refs. 3 and 91
CH ₂	CHene	1.540	634	Refs. 3 and 91
S	CH ₂	1.820	444	Refs. 4 and 91
CHar	CHar	1.40	938	Refs. 3 and 91
CHar	CH ₂	1.540	536	Refs. 3 and 91
CHar	CH ₃	1.540	536	Refs. 3 and 91
CH ₂ ar	CHar	1.40	938	Refs. 3 and 91
S	CHar	1.80384	527.951	This Work

Torsional potentials were fit to the TraPPE torsional function,

$$V_{\text{tor}} = c_0 + c_1 (1 + \cos \phi) + c_2 (1 - \cos 2\phi) + c_3 (1 + \cos 3\phi). \quad (2.9)$$

For the penultimate thiolate ligands, the model molecule used was 2-Butene-1-thiol, for which one bend angle (S–CH₂–CHene) was scanned to fit an equilibrium angle and force constant, as well as one torsion (S–CH₂–CHene–CHene). The parameters for these two potentials also served as model for the longer conjugated thiolate ligands which require bend angle parameters for (S–CH₂–CHar) and torsion

parameters for (S–CH₂–CChar–CChar).

For the C_4 conjugated thiolate ligands, the model molecule for the quantum mechanical calculations was 1,3-Butadiene-1-thiol. This ligand required fitting one bond (S–CChar), and one bend angle (S–CChar–CChar).

The geometries of the model molecules were optimized prior to performing the constrained angle scans, and the fit values for the bond, bend, and torsional parameters were in relatively good agreement with similar parameters already present in TraPPE.

To derive suitable parameters for the thiolates adsorbed on Au(111) surfaces, we adopted the S parameters from Luedtke and Landman[5] and modified the parameters for the CTS atom to maintain charge neutrality in the molecule.

Other interactions between metal (Au) and non-metal atoms were adapted from an adsorption study of alkyl thiols on gold surfaces by Vlugt, *et al.*[6] They fit an effective pair-wise Lennard-Jones form of potential parameters for the interaction between Au and pseudo-atoms CH_x and S based on a well-established and widely-used effective potential of Hautman and Klein for the Au(111) surface.[7] All simulations were carried out with the open source molecular dynamics package, OpenMD.[94, 95]

2.3.4 Simulation Protocol

Gold nanospheres with radii ranging from 10 - 25 Å were created from a bulk fcc lattice and were thermally equilibrated prior to the addition of ligands. A 50% coverage of ligands (based on coverages reported by Badia, *et al.*[85]) was placed on the surface of the equilibrated nanoparticles using Packmol[96]. Three lengths for the straight-chain ligands, C_4 , C_8 , and C_{12} , differentiated by the number of carbons in the chains are used in this study. Additionally, to explore the effects of ligand flexibility, three levels of ligand “stiffness” are examined. The most flexible chain

TABLE 2.3

Bend angle parameters. The central atom in the bend is atom j .

i	j	k	θ_0 (°)	k_{bend} (kcal/mol/rad 2)	source
CH ₂	CH ₂	S	114.0	124.20	Ref. 4
CH ₃	CH ₂	CH ₂	114.0	124.20	Ref. 4
CH ₂	CH ₂	CH ₂	114.0	124.20	Ref. 4
CHene	CHene	CH ₃	119.7	139.94	Ref. 3
CHene	CHene	CH ₂	119.7	139.94	Ref. 3
CH ₂	CH ₂	CHene	114.0	124.20	Ref. 3
Char	Char	Char	120.0	126.0	Refs. 3 and 91
Char	Char	CH ₂	120.0	140.0	Refs. 3 and 91
Char	Char	CH ₃	120.0	140.0	Refs. 3 and 91
Char	Char	CH ₂ ar	120.0	126.0	Refs. 3 and 91
S	CH ₂	CHene	109.97	127.37	This work
S	CH ₂	Char	109.97	127.37	This work
S	Char	Char	123.911	138.093	This work

is a fully saturated alkanethiolate, while moderate rigidity is introduced using an alkene thiolate with one double bond in the penultimate (solvent-facing) carbon-carbon location. The most rigid ligands are fully-conjugated chains where all of the carbons are represented with conjugated (aryl) united-atom carbon atoms (Char or terminal CH₂ar).

The nanoparticle / ligand complexes were thermally equilibrated to allow for ligand conformational flexibility. Packmol was then used to solvate the structures

TABLE 2.4

Torsion parameters. The central atoms for each torsion are atoms j and k , and wildcard atom types are denoted by “X”. All c_n parameters have units of kcal/mol. The torsions around carbon-carbon double bonds are harmonic and assume a trans (180°) geometry. The force constant for this torsion is given in $\text{kcal mol}^{-1}\text{degrees}^{-2}$.

i	j	k	l	c_0	c_1	c_2	c_3	source
CH ₃	CH ₂	CH ₂	CH ₂	0.0	0.7055	-0.13551	1.5725	Ref. 2
CH ₂	CH ₂	CH ₂	CH ₂	0.0	0.7055	-0.13551	1.5725	Ref. 2
CH ₂	CH ₂	CH ₂	S	0.0	0.7055	-0.13551	1.5725	Ref. 4
X	CHene	CHene	X	$V = \frac{0.008112}{2}(\phi - 180.0)^2$				Ref. 3
X	Char	Char	X					
CH ₂	CH ₂	CHene	CHene	1.368	0.1716	-0.2181	-0.56081	Ref. 3
CH ₂	CH ₂	CH ₂	CHene	0.0	0.7055	-0.13551	1.5725	Ref. 3
CHene	CHene	CH ₂	S	3.20753	0.207417	-0.912929	-0.958538	This work
Char	Char	CH ₂	S	3.20753	0.207417	-0.912929	-0.958538	This work

inside a spherical droplet of hexane. The thickness of the solvent layer was chosen to be at least $1.5 \times$ the combined radius of the nanoparticle / ligand structure. The fully solvated system was equilibrated for at least 1 ns using the “Langevin Hull” algorithm to apply 50 atm of pressure and a target temperature of 250 K.[1] Typical system sizes ranged from 18,310 united atom sites for the 10 Å particles with C_4 ligands to 89,490 sites for the 25 Å particles with C_{12} ligands. Figure 2.2 shows one of the solvated 25 Å nanoparticles passivated with the C_{12} alkane thiolate ligands. Once equilibrated, thermal fluxes were applied for 1 ns, until stable temperature

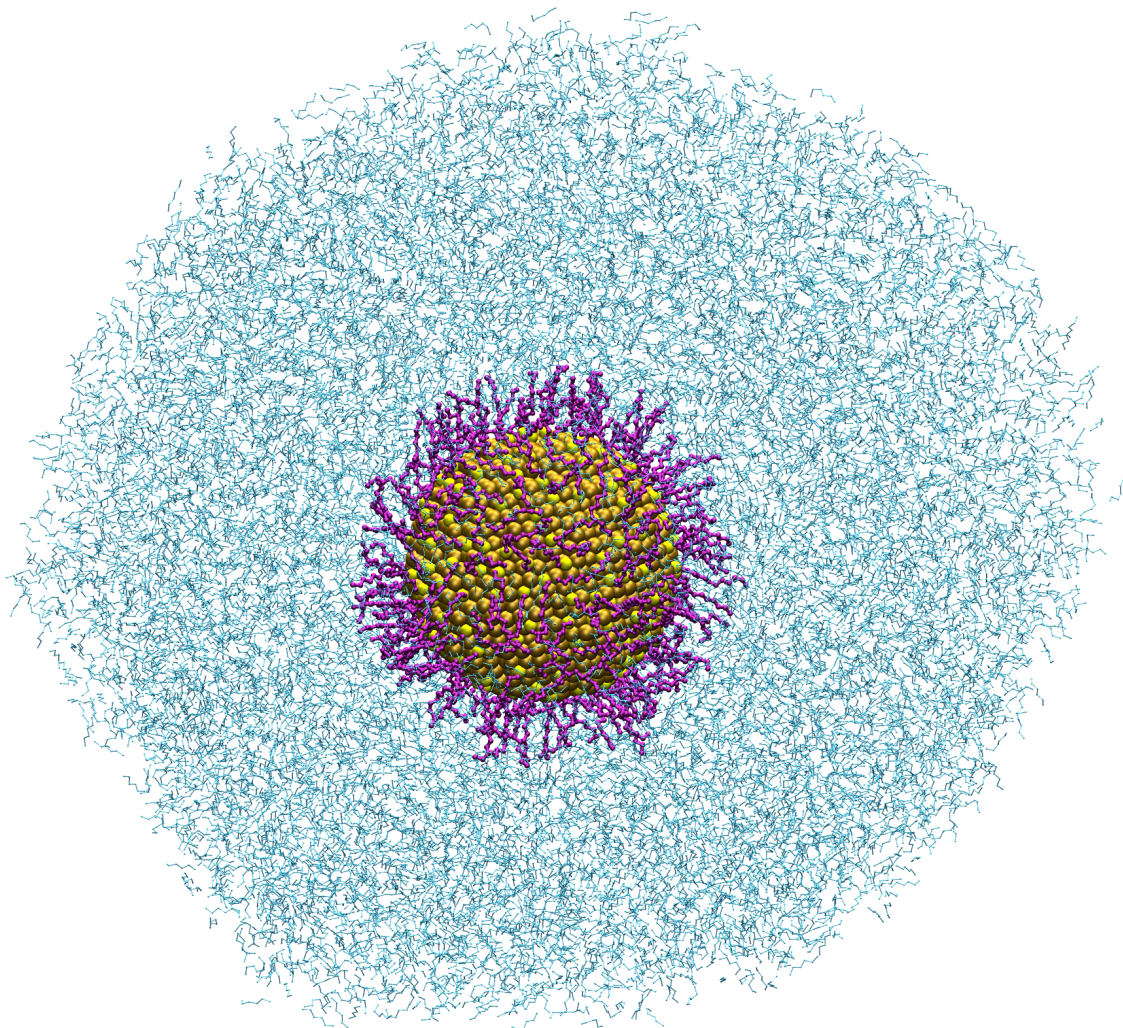


Figure 2.2. A 25 \AA radius gold nanoparticle protected with a half-monolayer of TraPPE-UA dodecanethiolate (C_{12}) ligands and solvated in TraPPE-UA hexane. The interfacial thermal conductance is computed by applying a kinetic energy flux between the nanoparticle and an outer shell of solvent.

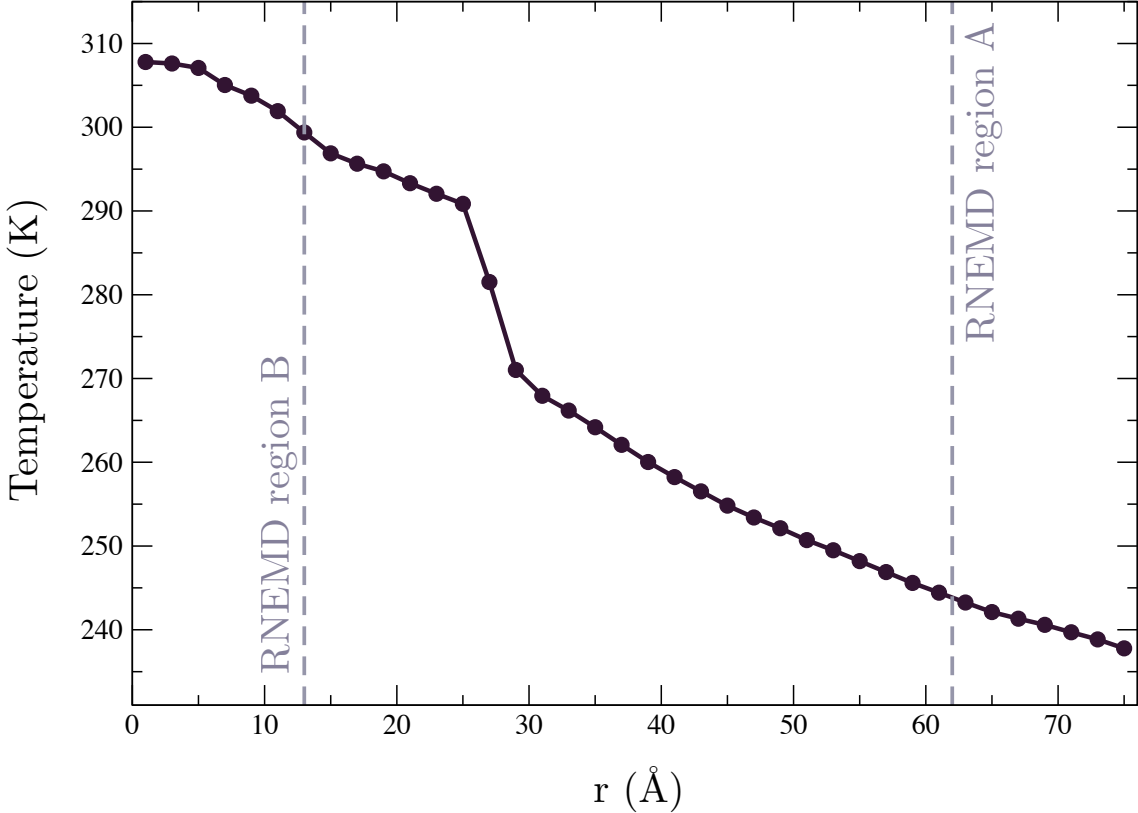


Figure 2.3. Radial temperature profile for a 25 Å radius particle protected with a 50% coverage of TraPPE-UA butanethiolate (C_4) ligands and solvated in TraPPE-UA hexane. A kinetic energy flux is applied between RNEMD region A and RNEMD region B. The size of the temperature discontinuity at the interface is governed by the interfacial thermal conductance.

gradients had developed (see Figure 2.3). Systems were run under moderate pressure (50 atm) with an average temperature (250K) that maintained a compact solvent cluster and avoided formation of a vapor layer near the heated metal surface. Pressure was applied to the system via the non-periodic “Langevin Hull” algorithm.[1] However, thermal coupling to the external temperature bath was removed to avoid interference with the imposed RNEMD flux.

Although the VSS-RNEMD moves conserve *total* angular momentum and energy, systems which contain a metal nanoparticle embedded in a significant volume of

solvent will still experience nanoparticle diffusion inside the solvent droplet. To aid in measuring an accurate temperature profile for these systems, a single gold atom at the origin of the coordinate system was assigned a mass $10,000 \times$ its original mass. The bonded and nonbonded interactions for this atom remain unchanged and the heavy atom is excluded from the RNEMD velocity scaling. The only effect of this gold atom is to effectively pin the nanoparticle at the origin of the coordinate system, thereby preventing translational diffusion of the nanoparticle due to Brownian motion.

To provide statistical independence, five separate configurations were simulated for each particle radius and ligand. The structures were unique, starting at the point of ligand placement, in order to sample multiple surface-ligand configurations.

2.4 Results

We modeled four sizes of nanoparticles ($R = 10, 15, 20,$ and 25 \AA). The smallest particle size produces the lowest interfacial thermal conductance values for most of the of protecting groups (Figure 2.4). Between the other three sizes of nanoparticles, there is no systematic dependence of the interfacial thermal conductance on the nanoparticle size. It is likely that the differences in local curvature of the nanoparticle sizes studied here do not disrupt the ligand packing and behavior in drastically different ways.

Unlike a previous study of varying thiolate ligand chain lengths on planar Au(111) surfaces, the interfacial thermal conductance of ligand-protected nanospheres exhibits a distinct dependence on the ligand identity.⁶ A half-monolayer coverage of ligands yields interfacial conductance that is strongly dependent on both ligand length and flexibility.

There are many factors that could be playing a role in the ligand-dependent conductuance. The sulfur-gold interaction is particularly strong, and the presence of the ligands can easily disrupt the crystalline structure of the gold at the surface of

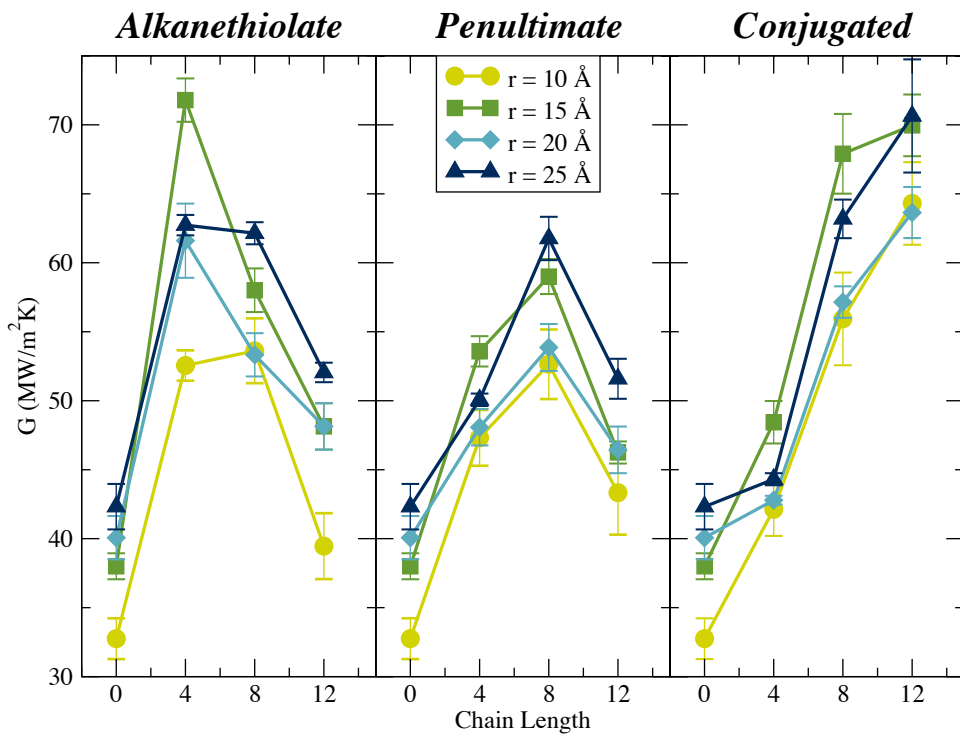


Figure 2.4. Interfacial thermal conductance (G) values for 4 sizes of solvated nanoparticles that are bare or protected with a 50% coverage of C₄, C₈, or C₁₂ thiolate ligands. Ligands of different flexibility are shown in separate panels. The middle panel indicates ligands which have a single carbon-carbon double bond in the penultimate position.

the particles, providing more efficient scattering of phonons into the ligand / solvent layer. This effect would be particularly important at small particle sizes.

In previous studies of mixed-length ligand layers with full coverage, we observed that ligand-solvent alignment was an important factor for heat transfer into the solvent. With high surface curvature and lower effective coverages, ligand behavior also becomes more complex. Some chains may be lying down on the surface, and solvent may not be penetrating the ligand layer to the same degree as in the planar surfaces.

Additionally, the ligand flexibility directly alters the vibrational density of states for the layer that mediates the transfer of phonons between the metal and the solvent. This could be a partial explanation for the observed differences between the fully conjugated and more flexible ligands.

In the following sections details on how I measure surface corrugation, solvent-ligand interpenetration, and ordering of the solvent and ligand at the surfaces of the nanospheres are provided. Followed by an investigation of the overlap between vibrational densities of states for the various ligands.

2.4.1 Corrugation of the Particle Surface

The bonding sites for thiols on gold surfaces have been studied extensively and include configurations beyond the traditional atop, bridge, and hollow sites found on planar surfaces. In particular, the deep potential well between the gold atoms and the thiolate sulfur atoms leads to insertion of the sulfur into the gold lattice and displacement of interfacial gold atoms. The degree of ligand-induced surface restructuring may have an impact on the interfacial thermal conductance and is an important phenomenon to quantify.

Henz, *et al.*[84] used the metal density as a function of radius to measure the degree of mixing between the thiol sulfurs and surface gold atoms at the edge of a

nanoparticle. Although metal density is important, disruption of the local crystalline ordering would also have a large effect on the phonon spectrum in the particles. To measure this effect, the fraction of gold atoms exhibiting local fcc ordering as a function of radius to describe the ligand-induced disruption of the nanoparticle surface is used.

The local bond orientational order can be described using the method of Steinhardt *et al.*[97] The local bonding environment, $\bar{q}_{\ell m}$, for each atom in the system is determined by averaging over the spherical harmonics between that atom and each of its neighbors,

$$\bar{q}_{\ell m} = \sum_i Y_{\ell}^m(\theta_i, \phi_i) \quad (2.10)$$

where θ_i and ϕ_i are the relative angular coordinates of neighbor i in the laboratory frame. A global average orientational bond order parameter, $\bar{Q}_{\ell m}$, is the average over each $\bar{q}_{\ell m}$ for all atoms in the system. To remove the dependence on the laboratory coordinate frame, the third order rotationally invariant combination of $\bar{Q}_{\ell m}$, \hat{w}_{ℓ} , is utilized here.[97, 98]

For $\ell = 4$, the ideal face-centered cubic (fcc), body-centered cubic (bcc), hexagonally close-packed (hcp), and simple cubic (sc) local structures exhibit \hat{w}_4 values of -0.159, 0.134, 0.159, and 0.159, respectively. Because \hat{w}_4 exhibits an extreme value for fcc structures, it is ideal for measuring local fcc ordering. The spatial distribution of \hat{w}_4 local bond orientational order parameters, $p(\hat{w}_4, r)$, can provide information about the location of individual atoms that are central to local fcc ordering.

The fraction of fcc-ordered gold atoms at a given radius in the nanoparticle,

$$f_{\text{fcc}}(r) = \int_{-\infty}^{w_c} p(\hat{w}_4, r) d\hat{w}_4 \quad (2.11)$$

is described by the distribution of the local bond orientational order parameters, $p(\hat{w}_4, r)$, and w_c , a cutoff for the peak \hat{w}_4 value displayed by fcc structures. A w_c

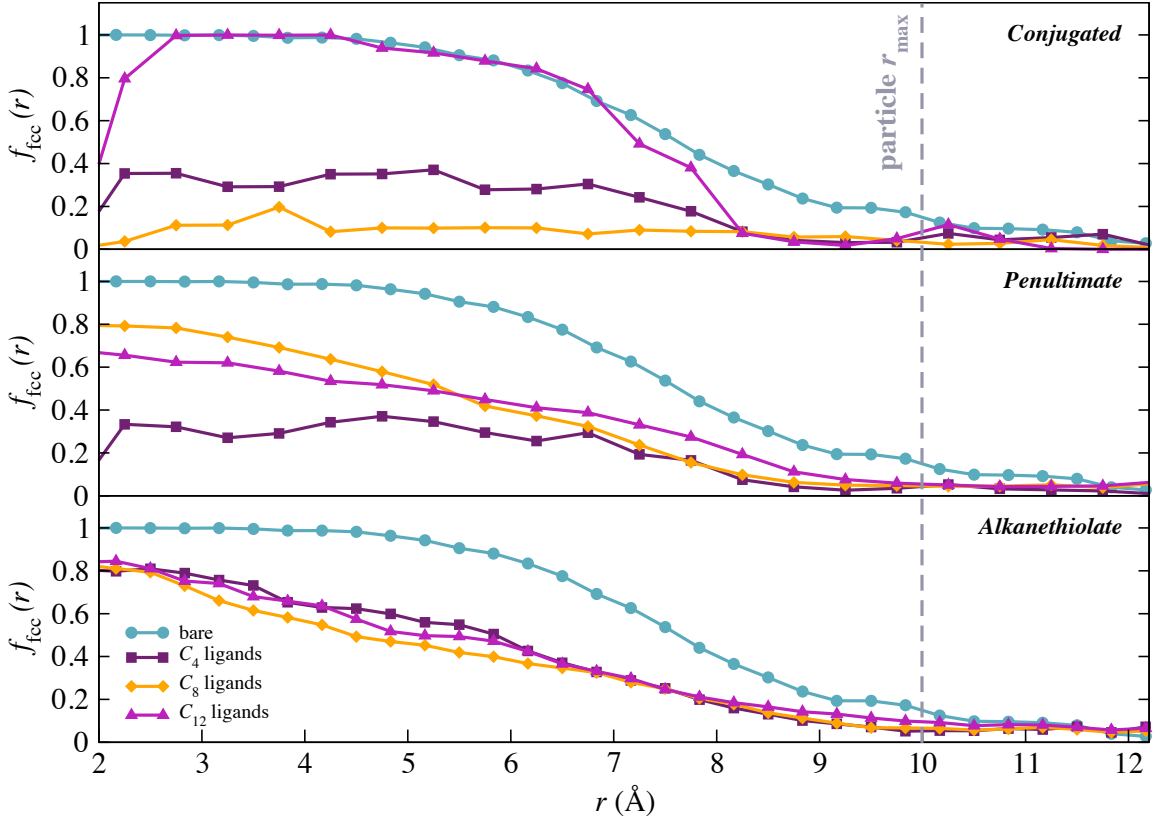


Figure 2.5. Fraction of gold atoms with fcc ordering as a function of radius for a 10 Å radius nanoparticle. The decreased fraction of fcc-ordered atoms in ligand-protected nanoparticles relative to bare particles indicates restructuring of the nanoparticle surface by the thiolate sulfur atoms.

value of -0.12 was chosen to isolate the fcc peak in \hat{w}_4 .

As illustrated in Figure 2.5, the presence of ligands decreases the fcc ordering of the gold atoms at the nanoparticle surface. For the smaller nanoparticles, this disruption extends into the core of the nanoparticle, indicating widespread disruption of the lattice.

The thickness of the disrupted nanoparticle surface can be described by defining a corrugation factor, c , as the ratio of the radius at which the fraction of gold atoms with fcc ordering is 0.9 and the radius at which the fraction is 0.5.

$$c = 1 - \frac{r(f_{\text{fcc}} = 0.9)}{r(f_{\text{fcc}} = 0.5)} \quad (2.12)$$

A sharp interface will have a steep drop in f_{fcc} at the edge of the particle ($c \rightarrow 0$). In the opposite limit where the entire nanoparticle surface is restructured by ligands, the radius at which there is a high probability of fcc ordering moves dramatically inward ($c \rightarrow 1$).

The computed corrugation factors are shown in Figure 2.6 for bare nanoparticles and for ligand-protected particles as a function of ligand chain length. The largest nanoparticles are only slightly restructured by the presence of ligands on the surface, while the smallest particle ($r = 10 \text{ \AA}$) exhibits significant disruption of the original fcc ordering when covered with a half-monolayer of thiol ligands.

Since the thiolate ligands do not significantly alter the larger particle crystallinity, the surface corrugation does not seem to be a likely candidate to explain the large increase in thermal conductance at the interface when ligands are added.

2.4.2 Orientation of Ligand Chains

Previous theoretical work on heat conduction through alkane chains has shown that short chains are dominated by harmonic interactions, where the energy is carried ballistically through the chain.[99] As the saturated ligand chain length increases in length, it exhibits significantly more conformational flexibility. Thus, different lengths of ligands should favor different chain orientations on the surface of the nanoparticle, and can localize the ligand vibrational density of states close to the particle, lowering the effectiveness of the heat conduction.[99] To determine the distribution of ligand orientations relative to the particle surface the probability of finding a ligand with a

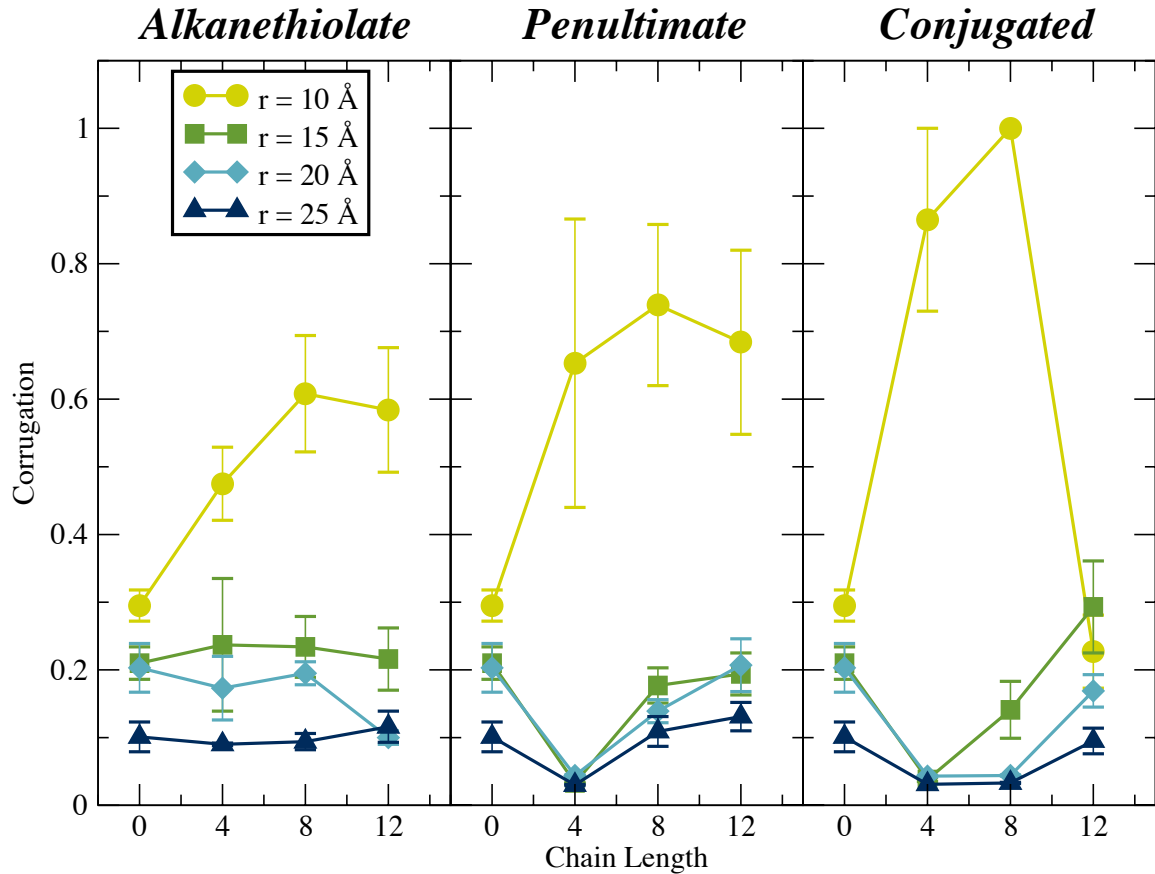


Figure 2.6. Computed corrugation values for 4 sizes of solvated nanoparticles that are bare or protected with a 50% coverage of C₄, C₈, or C₁₂ thiolate ligands. The smallest (10 Å) particles show significant disruption to their crystal structures, and the length and stiffness of the ligands is a contributing factor to the surface disruption.

particular orientation relative to the surface normal of the nanoparticle is examined,

$$\cos(\theta) = \frac{\vec{r}_i \cdot \hat{u}_i}{|\vec{r}_i||\hat{u}_i|} \quad (2.13)$$

where \vec{r}_i is the vector between the cluster center of mass and the sulfur atom on ligand molecule i , and \hat{u}_i is the vector between the sulfur atom and CH_3 pseudo-atom on ligand molecule i . As depicted in Figure 2.7, $\theta \rightarrow 180^\circ$ for a ligand chain standing upright on the particle ($\cos(\theta) \rightarrow -1$) and $\theta \rightarrow 90^\circ$ for a ligand chain lying down on the surface ($\cos(\theta) \rightarrow 0$). As the thiolate alkane chain increases in length and becomes more flexible, the ligands are more willing to lie down on the nanoparticle surface and exhibit increased population at $\cos(\theta) = 0$.

An order parameter describing the average ligand chain orientation relative to the nanoparticle surface is available using the second order Legendre parameter,

$$P_2 = \left\langle \frac{1}{2} (3 \cos^2(\theta) - 1) \right\rangle \quad (2.14)$$

Ligand populations that are perpendicular to the particle surface have P_2 values of 1, while ligand populations lying flat on the nanoparticle surface have P_2 values of -0.5 . Disordered ligand layers will exhibit mean P_2 values of 0. As shown in Figure 2.8 the ligand P_2 values approaches 0 as ligand chain length – and ligand flexibility – increases.

2.4.3 Orientation of Interfacial Solvent

Similarly, I examined the distribution of *hexane* molecule orientations relative to the particle surface using the same angular analysis utilized for the ligand chain orientations. In this case, \vec{r}_i is the vector between the particle center of mass and one of the CH_2 pseudo-atoms in the middle of hexane molecule i and \hat{u}_i is the vector between the two CH_3 pseudo-atoms on molecule i . Since only the orientation of

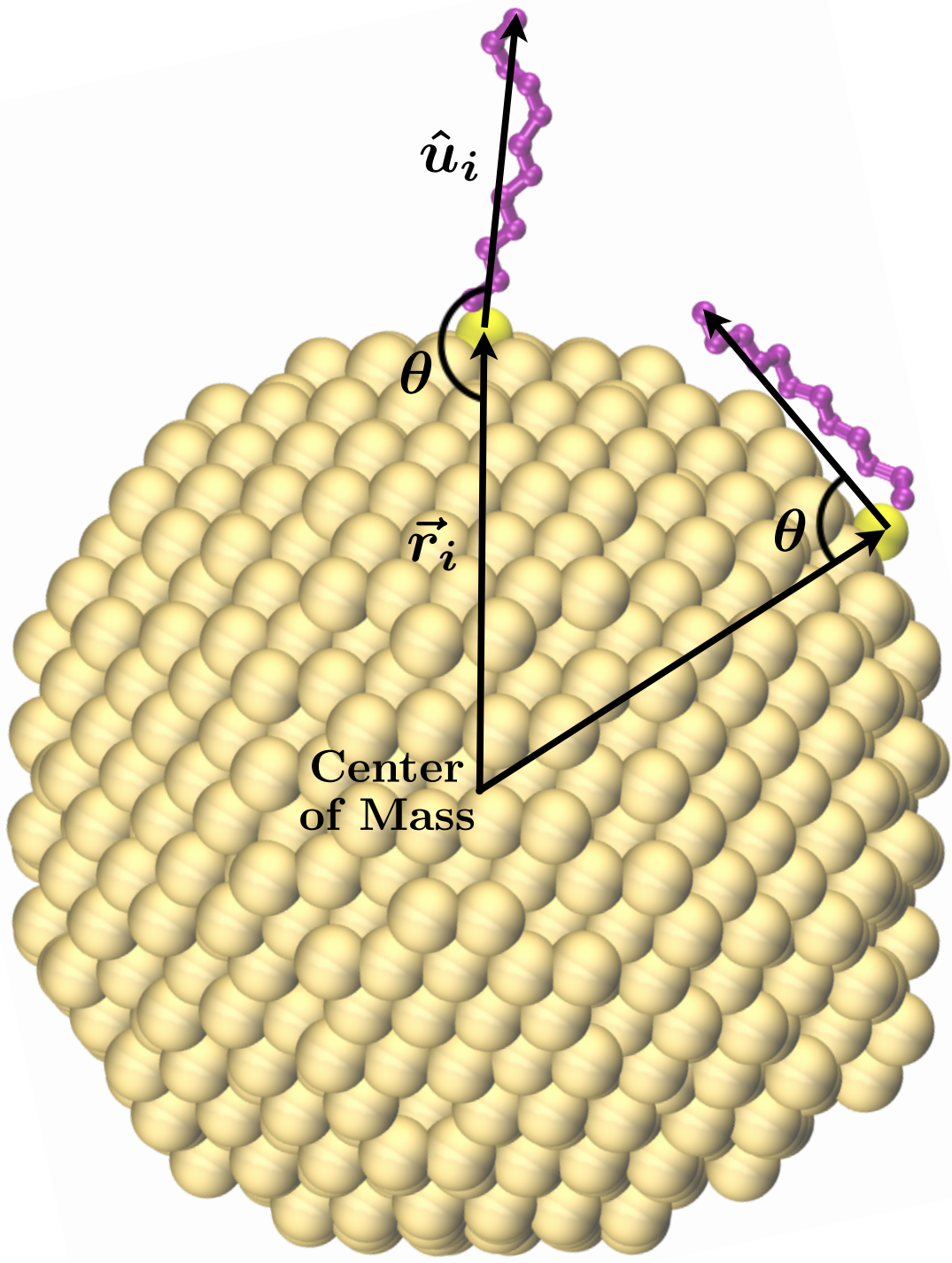


Figure 2.7. The two extreme cases of ligand orientation relative to the nanoparticle surface: the ligand completely outstretched ($\cos(\theta) = -1$) and the ligand fully lying down on the particle surface ($\cos(\theta) = 0$).

solvent molecules near the ligand layer is of interest, I select only the hexane molecules within a specific r -range, between the edge of the particle and the end of the ligand chains. A large population of hexane molecules with $\cos(\theta) \sim \pm 1$ would indicate interdigititation of the solvent molecules between the upright ligand chains. A more random distribution of $\cos(\theta)$ values indicates a disordered arrangement of solvent molecules near the particle surface. Again, P_2 order parameter values provide a population analysis for the solvent that is close to the particle surface.

The average orientation of the interfacial solvent molecules is notably flat on the *bare* nanoparticle surfaces. This blanket of hexane molecules on the particle surface may act as an insulating layer, increasing the interfacial thermal resistance. As the length (and flexibility) of the ligand increases, the average interfacial solvent P_2 value approaches 0, indicating a more random orientation of the ligand chains. The average orientation of solvent within the C_8 and C_{12} ligand layers is essentially random. Solvent molecules in the interfacial region of C_4 ligand-protected nanoparticles do not lie as flat on the surface as in the case of the bare particles, but are not as randomly oriented as the longer ligand lengths.

These results are particularly interesting in light of previous work by Stocker *et al*[55], where solvent molecules readily filled the vertical gaps between neighboring ligand chains and there was a strong correlation between ligand and solvent molecular orientations. It appears that the introduction of surface curvature and a lower ligand packing density creates a disordered ligand layer that lacks well-formed channels for the solvent molecules to occupy.

2.4.4 Solvent Penetration of Ligand Layer

The extent of ligand – solvent interaction is also determined by the degree to which these components occupy the same region of space adjacent to the nanoparticle. The radial density profiles of these components help determine this degree of interaction.

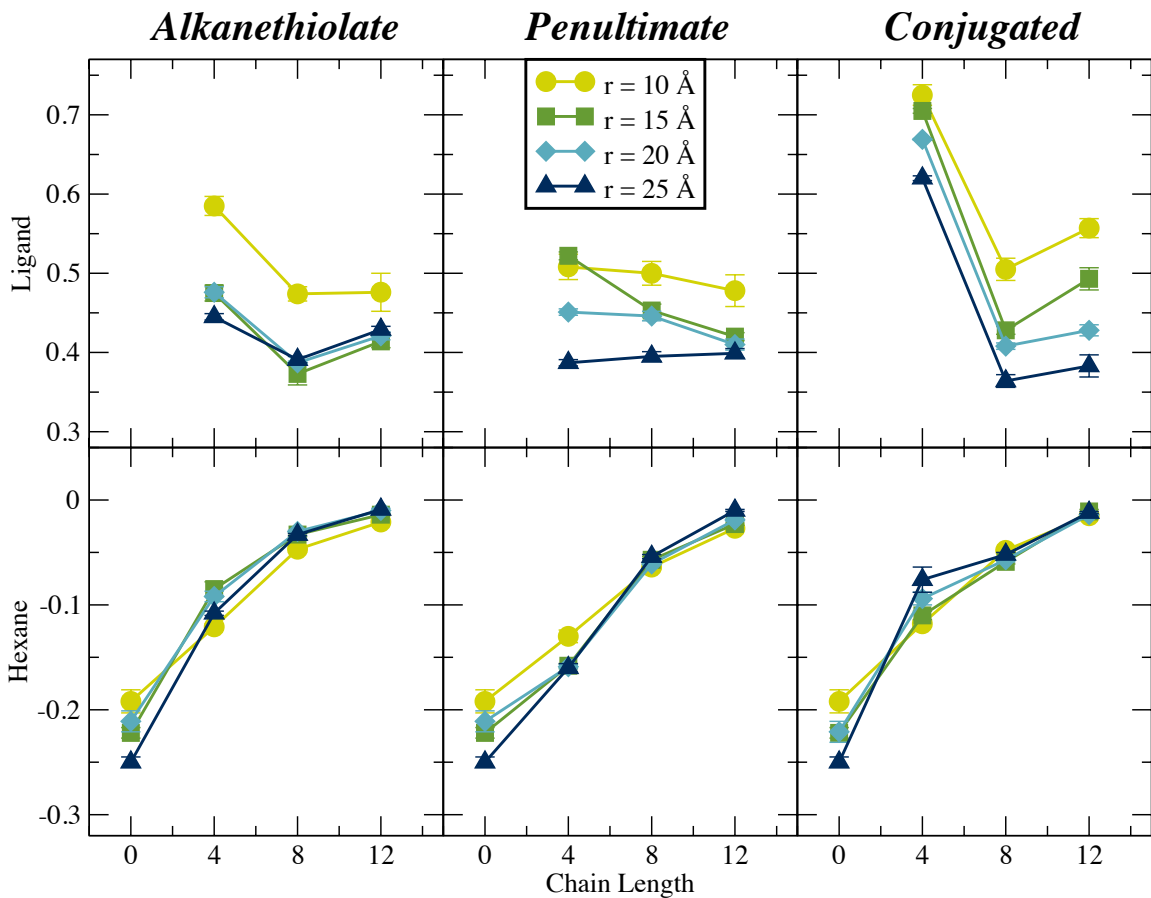


Figure 2.8. Computed ligand and interfacial solvent orientational P_2 values for 4 sizes of solvated nanoparticles that are bare or protected with a 50% coverage of C_4 , C_8 , or C_{12} alkanethiolate ligands. Increasing stiffness of the ligand orients these molecules normal to the particle surface, while the length of the ligand chains works to prevent solvent from lying flat on the surface.

Figure 2.9 shows representative density profiles for solvated 25 Å radius nanoparticles with no ligands, and with a 50% coverage of C₄, C₈, and C₁₂ thiolates.

The differences between the radii at which the hexane surrounding the ligand-covered particles reaches bulk density correspond nearly exactly to the differences between the lengths of the ligand chains. Beyond the edge of the ligand layer, the solvent reaches its bulk density within a few angstroms. The differing shapes of the density curves indicate that the solvent is increasingly excluded from the ligand layer as the chain length increases.

The conjugated ligands create a distinct solvent shell within the ligand layer and also allow significantly more solvent to penetrate close to the particle. A density overlap parameter can be defined,

$$O_{l-s} = \frac{1}{V} \int_0^{r_{\max}} 4\pi r^2 \frac{4\rho_l(r)\rho_s(r)}{(\rho_l(r) + \rho_s(r))^2} dr \quad (2.15)$$

where $\rho_l(r)$ and $\rho_s(r)$ are the ligand and solvent densities at a radius r , and V is the total integration volume ($V = 4\pi r_{\max}^3/3$). The fraction in the integrand is a dimensionless quantity that is unity when ligand and solvent densities are identical at radius r , but falls to zero when either of the two components are excluded from that region.

The density overlap parameters are shown in Figure 2.10. The calculated overlap parameters indicate that the conjugated ligand allows for the most solvent penetration close to the particle, and that shorter chains generally permit greater solvent penetration in the interfacial region. Increasing overlap can certainly allow for enhanced thermal transport, but this is clearly not the only contributing factor. Even when the solvent and ligand are in close physical contact, there must also be good vibrational overlap between the phonon densities of states in the ligand and solvent to transmit vibrational energy between the two materials.

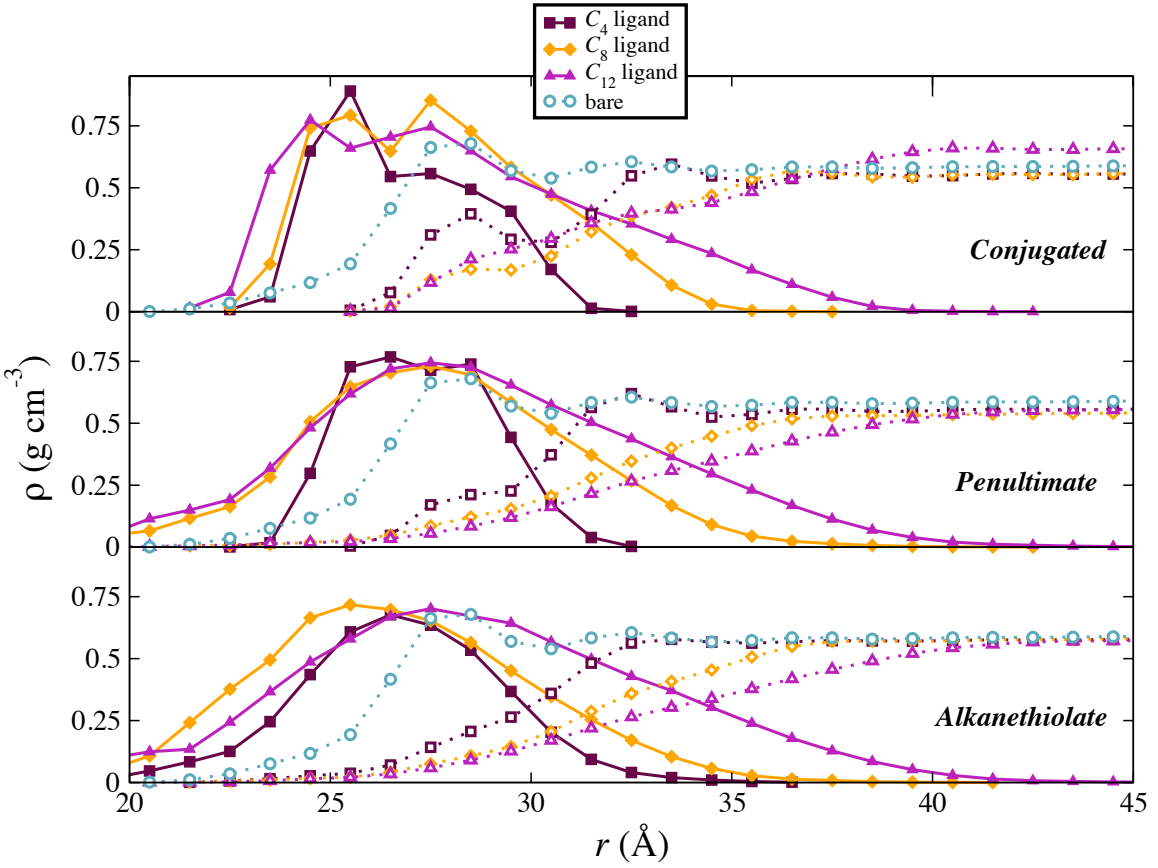


Figure 2.9. Radial density profiles for 25 Å radius nanoparticles with no ligands (circles), C_4 ligands (squares), C_8 ligands (diamonds), and C_{12} ligands (triangles). Ligand density is indicated with filled symbols, solvent (hexane) density is indicated with open symbols. As ligand chain length increases, the nearby solvent is excluded from the ligand layer. The conjugated ligands (upper panel) can create a separated solvent shell within the ligand layer and also allow significantly more solvent to penetrate close to the particle.

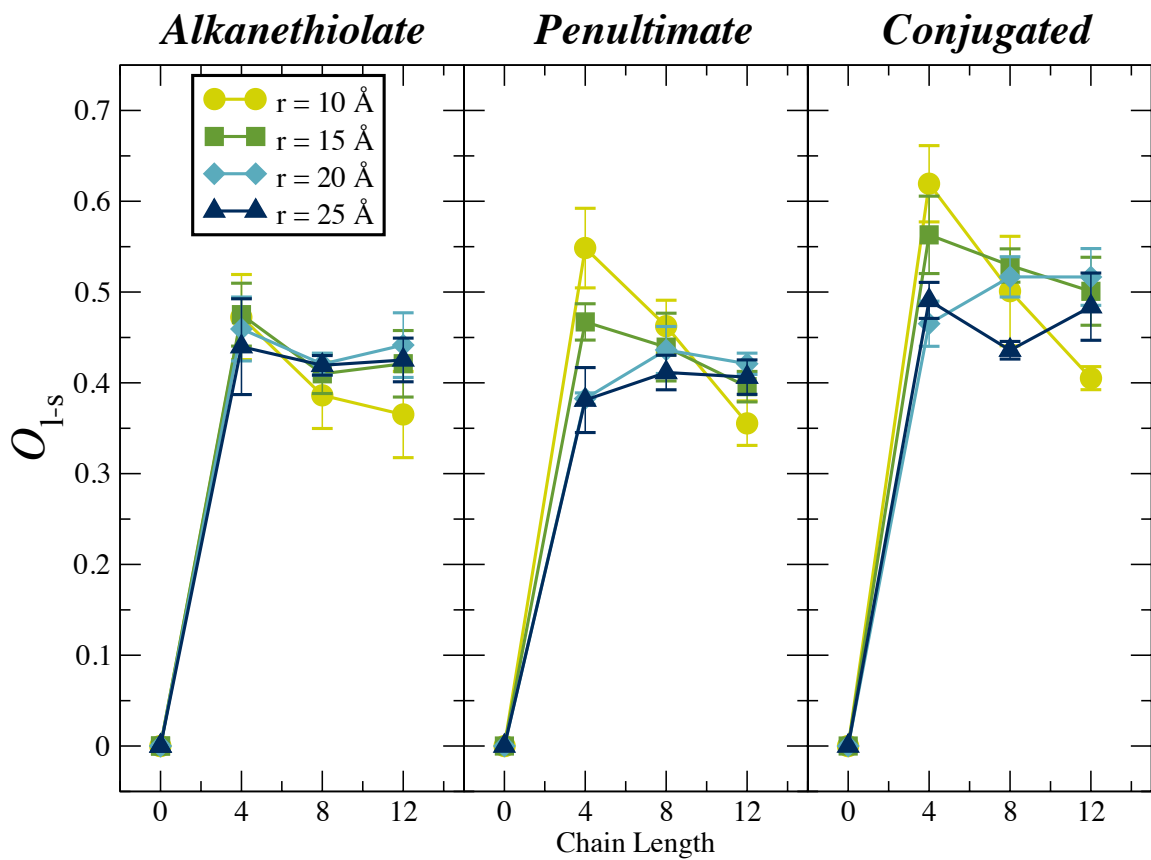


Figure 2.10. Density overlap parameters (O_{l-s}) for solvated nanoparticles protected by thiolate ligands. In general, the rigidity of the fully-conjugated ligands provides the easiest route for solvent to enter the interfacial region. Additionally, shorter chains allow a greater degree of solvent penetration of the ligand layer.

2.4.5 Ligand-mediated Vibrational Overlap

In phonon scattering models for interfacial thermal conductance,[19, 20, 78, 100, 101] the frequency-dependent transmission probability ($t_{a \rightarrow b}(\omega)$) predicts phonon transfer between materials a and b . Many of the models for interfacial phonon transmission estimate this quantity using the phonon density of states and group velocity, and make use of a Debye model for the density of states in the solid.

A consensus picture is that in order to transfer the energy carried by an incoming phonon of frequency ω on the a side, the phonon density of states on the b side must have a phonon of the same frequency. The overlap of the phonon densities of states, particularly at low frequencies, therefore contributes to the transfer of heat. Phonon scattering must be done in a direction perpendicular to the interface. In the geometries described here, there are two interfaces (particle \rightarrow ligand, and ligand \rightarrow solvent), and the vibrational overlap between the ligand and the other two components is relevant to heat transfer.

To estimate the relevant densities of states, I have projected the velocity of each atom i in the region of the interface onto a direction normal to the interface. For the nanosphere geometries studied here, the normal direction depends on the instantaneous position of the atom relative to the center of mass of the particle.

$$v_{\perp}(t) = \mathbf{v}(t) \cdot \frac{\mathbf{r}(t)}{|\mathbf{r}(t)|} \quad (2.16)$$

The quantity $v_{\perp}(t)$ measures the instantaneous velocity of an atom in a direction perpendicular to the nanoparticle interface. In the interfacial region, the autocorrelation function of these velocities,

$$C_{\perp}(t) = \langle v_{\perp}(t) \cdot v_{\perp}(0) \rangle, \quad (2.17)$$

will include contributions from all of the phonon modes present at the interface. The Fourier transform of the time-symmetrized autocorrelation function provides an estimate of the vibrational density of states,[102]

$$\rho(\omega) = \frac{1}{\tau} \int_{-\tau/2}^{\tau/2} C_{\perp}(t) e^{-i\omega t} dt. \quad (2.18)$$

Here τ is the total observation time for the autocorrelation function. In Figure 2.11 shows the low-frequency region of the normalized vibrational densities of states for the three chemical components (gold nanoparticle, C_{12} ligands, and interfacial solvent). The double bond in the penultimate location is a small perturbation on ligands of this size, and that is reflected in relatively similar spectra in the lower panels. The fully conjugated ligand, however, shifts the peak in the lowest frequency band from $\sim 29\text{cm}^{-1}$ to $\sim 55\text{cm}^{-1}$, yielding significant overlap with the density of states in the nanoparticle. This ligand increases the overlap with the solvent density of states in a band between 280 and 380 cm^{-1} . This provides some physical basis for the high interfacial conductance observed for the fully conjugated C_8 and C_{12} ligands.

The similarity between the density of states for the alkanethiolate and penultimate ligands explains why the interfacial conductance is nearly the same for these two ligands, particularly at longer chain lengths.

2.5 Discussion

The chemical bond between the metal and the ligand introduces vibrational overlap that is not present between the bare metal surface and solvent. Thus, regardless of ligand identity or chain length, the presence of a half-monolayer ligand coverage yields a higher interfacial thermal conductance value than the bare nanoparticle. The mechanism for the varying conductance for the different ligands is somewhat less clear. Ligand-based alterations to vibrational density of states is a major con-

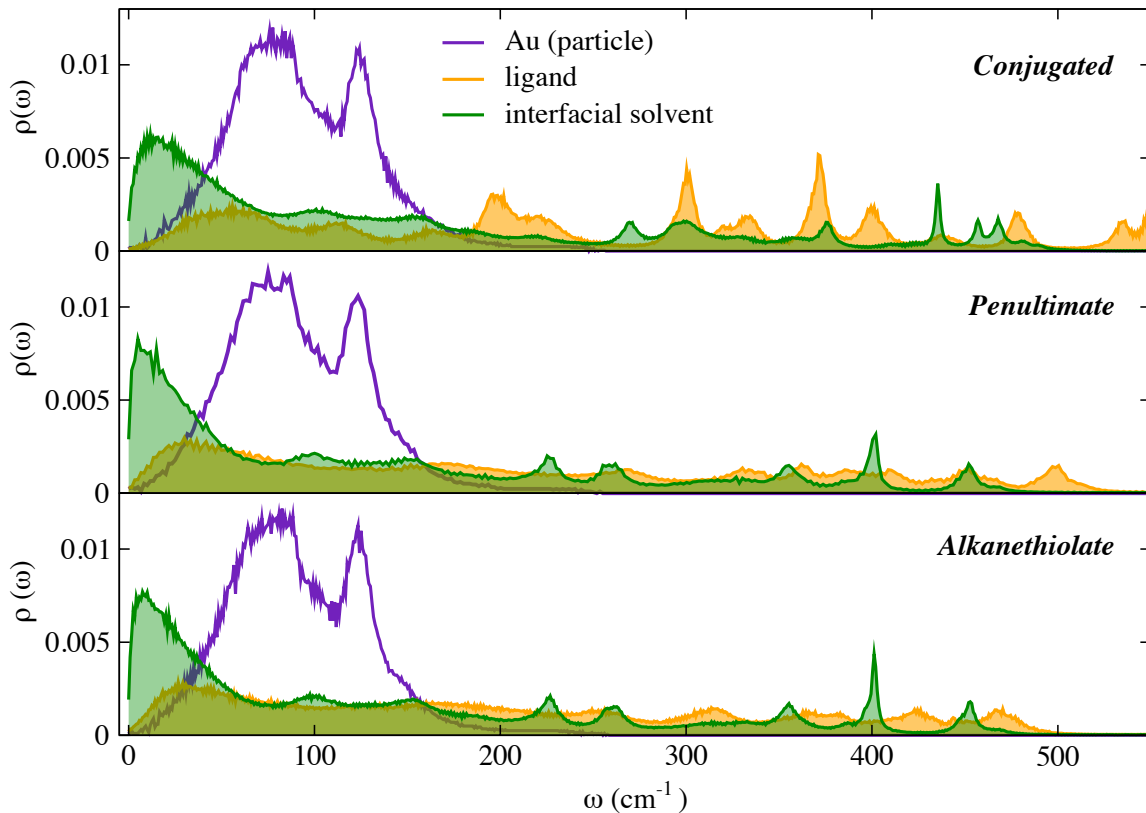


Figure 2.11. The low frequency portion of the vibrational density of states for three chemical components (gold nanoparticles, C_{12} ligands, and hexane solvent). These densities of states were computed using the velocity autocorrelation functions for atoms in the interfacial region, constructed with velocities projected onto a direction normal to the interface.

tributor, but some of the ligands can disrupt the crystalline structure of the smaller nanospheres, while others can re-order the interfacial solvent and alter the interpenetration profile between ligand and solvent chains. Further work to separate the effects of ligand-solvent interpenetration and surface reconstruction is clearly needed for a complete picture of the heat transport in these systems.

CHAPTER 3

THERMAL TRANSPORT IS INFLUENCE By NANOPARTICLE SHAPE

3.1 Abstract

Molecular dynamics simulations were performed to model the interfacial thermal conductance (G) from bare gold nanoparticles (icosahedral, cuboctahedral, and spherical) to a hexane solvent. The computed conductance was found to depend not only on particle shape, but also on the size of the nanoparticles, particularly for nanospheres. These results are compared with conductance out of the planar facets: (111), (100), and (110); all commonly exhibited in small patches by the spherical particles. Undercoordination of the surface atoms and the vibrational density of states in the icosahedra explain some of these observations. The exposed surfaces of icosahedral particles are dominated by (111) facets with 9-coordinated gold atoms. Cuboctahedral particles are dominated by the (100) and (111) facets with 8- and 9-coordinated surface atoms, respectively. The nanospheres approach a constant surface density of 6-9 coordinated sites at large particle sizes, and these surface atoms play a large role in the conductance to the solvent. The surface-normal vibrational densities of states were used to explain a simple surface undercoordination model, which shows a size-dependent enhancement of low-frequency coupling to the solvent.

3.2 Introduction

Thermal transport between nanoparticles and their surrounding environments depends on many factors, including particle size,[57–61] composition,[62? , 63] surface

modification,[58, 60, 63? ? –68] surface supports,[69?] exposed surface facets,[66? ?] and the chemical details of the environment.[59, 63, 65, 67, 69? ? ? ?, 70] Particle morphology may also play a role in heat transfer out of nanostructures. This is the central question of this work – all other things being equal, will different particle morphologies yield different heat transfer properties to the solvent?

Tascini *et al.*[61] studied the curvature dependence of the interfacial thermal conductance for partially solvated nanospheres. They found an empirical relationship,

$$G(r) = G(\infty) + \frac{\delta}{r} \quad (3.1)$$

where $G(r)$ is the conductance out of a sphere of radius r , $G(\infty)$ is a parameter describing the infinite-radius limit of the conductance, and δ describes the approach to the infinite size limit. Notably, the Tascini *et al.* simulations predict a positive δ , where smaller particles exhibit high interfacial thermal conductance and approach an infinite surface limit that has lower thermal conductance to the solvent. This makes intuitive sense – one might expect the large particle limit to approach the behavior of flat interfaces.

To test this hypothesis, heat transfer out of gold nanospheres that were in direct contact with a molecular solvent have been computed. The spheres were cut out of an infinite FCC lattice and spanned a range of sizes. The spheres expose many surface facets including patches of the (111), (100), and (110) facets, due to the cuts in the underlying FCC lattice. The interfacial thermal conductance out of similarly-sized icosahedral particles that exhibit only (111) facets and cuboctahedral particles that display only (111) and (100) facets have been compared to the spheres. I have also compared the interfacial thermal conductance to flat interfaces that match the facets exposed on the surfaces of the spheres.

One possible explanation for an empirical relationship like Eq. (3.1) is that there

is a significant contribution to interfacial thermal conductance that depends on the surface area to volume ratio, suggesting a large role for the surface atoms. In previous work, the thermal conductance out of chemically-modified gold surfaces was examined via reverse nonequilibrium molecular dynamics (RNEMD). [56, 60, 64] In these studies, surfactants attached to the gold surfaces contained a strong gold – sulfur interaction that acted as a bridge for vibrational energy to travel to the ligand. Although the presence and density of the ligand layer has a large effect on the interfacial conductance, no clear trend was established regarding the size and curvature of the underlying nanoparticles. Previous studies from Tascini *et al.*[61] and Ong *et al.*[65] predict a decrease in the interfacial thermal conductance as the particle radius increases, although Ong *et al.*[65] and Zanjani *et al.*[57] predict higher thermal conductivity with increasing core diameter in nanocrystal arrays. However, if surface modifications dominate conductance, the presence of a moderate density of ligands will obscure the effects of particle curvature.

3.2.1 Size- and temperature-dependent particle morphologies

The nanoparticles simulated for this work ranged in size from 309 atoms to 14,993 atoms. Ercolelli *et al.*[?] annealed at temperatures from 400K to 1400K and found the dominant structures for different sizes of gold particles ($N = 100\text{--}900$ atoms). For $N = 100\text{--}200$, the structures were dominated by glassy clusters while for $N = 200\text{--}900$, the structures were predominantly cuboctahedral. Similarly, Myshlyavtsev and Stishenko found, when comparing gold nanostructures, a transition from a fully (111) icosahedral structure to a (100)-terminated cuboctahedral structures between 561 to 1,415 atoms, depending on the potential energy function.[?] Distinct vibrational densities of states have also been observed for the cuboctahedral clusters relative to icosahedra.[?]

In a study of the thermal stability of gold icosahedra, Wang *et al.*[?] found

that softening of the vertex and edge atoms occurs at $\approx 800\text{K}$. During this process they saw enhanced surface atom diffusion due to the mobility of the vertex and edge atoms.

The size range ($N = 300\text{-}15,000$) and temperatures (250K) for the calculations described here exhibit stable icosahedra with relatively low surface atom mobility, except for the smallest ($r = 18\text{-}22 \text{\AA}$) particles, which may be metastable relative to cuboctahedra.

3.2.2 Theory

Under the diffuse mismatch model (DMM), the thermal conductance at an interface between a and b can be approximated,

$$G_{ab} = \frac{1}{4\pi} \sum_p \int_{\omega} \int_{\theta} \int_{\phi} \hbar\omega \frac{\partial f}{\partial T} v_a \rho_a \tau_{ab} \cos \theta \sin \theta d\theta d\phi d\omega \quad (3.2)$$

where f is the Bose-Einstein distribution function, $v_a(\omega, p)$ is the group velocity (on side a) for a phonon characterized by frequency ω , moving in direction (θ, ϕ) with polarization p . The relevant material properties are the density of phonon states, $\rho_a(\omega, p)$ and the transmission probability, $\tau_{ab}(\omega, p)$, at the interface.[13, 19, 20]

The diffuse mismatch model has a number of significant issues, particularly when the Debye model is a poor representation of the density of states, or where there is a fictitious boundary between identical materials (where the DMM predicts a non-zero resistance).[13] There is also an assumption of detailed balance built-in to the model,[8] which requires the two sides to be at equilibrium. This assumption is violated under non-equilibrium conditions, as in the RNEMD simulations used here. Although the DMM is not quantitative, it does suggest a role for frequency-dependent phonon transmission at the interface and that isolating the frequencies of the phonons moving towards the interface could aid in understanding interfacial conductance.

Using atomic velocities projected in a direction normal to the interface,

$$v_i^\perp(t) = \mathbf{v}_i(t) \cdot \hat{\mathbf{n}}, \quad (3.3)$$

it is straightforward to compute vibrational power spectra,

$$\rho^\perp(\omega) = \frac{1}{\tau} \int_{-\tau/2}^{\tau/2} \langle v^\perp(t) \cdot v^\perp(0) \rangle e^{-i\omega t} dt \quad (3.4)$$

which have been averaged over direction and polarization, where τ is the total observation time for the autocorrelation function. This can be used to approximate the density of phonon states of the two materials near the interface, which can provide a clearer picture of vibrational communication between the two materials. By further restricting the density of states calculation to specific atoms at the metallic side of the interface, I hope to provide a mechanism for heat flow from the solid and into the surrounding liquid.

To compute interfacial thermal conductance values directly, reverse non-equilibrium molecular dynamics (RNEMD) simulations are utilized.[47, 49] RNEMD imposes an unphysical kinetic energy exchange between the center of the particle and a spherical shell of solvent that is well-separated from the interface. The system responds by creating a thermal gradient in the metal and solvent regions, and a temperature discontinuity at the interface between the particle and the solvent. The Kapitza resistance of the interface,

$$R_K = \frac{1}{G} = \frac{1}{q_r} \sum_i (T_{i+i} - T_i) 4\pi r_i^2, \quad (3.5)$$

is estimated by summing the individual thermal resistances of concentric spherical shells as the radius increases.[56] Here, T_i is the temperature of a shell with radius r_i , and q_r is the heat rate (the relevant measure of thermal transport in spherical

geometries). The heat rate is the surface area of the particle times that of the imposed flux. The interfacial thermal conductance of the interface, G is the inverse of the net Kapitza resistance. For interfaces of appreciable width, the relevant shells for measuring interfacial resistance are the largest shell that is unambiguously in the particle and the smallest shell that is unambiguously in the solvent.

For planar or periodic geometries, the interfacial thermal conductance can be similarly computed by imposing a non-physical flux between two separated slabs in the simulation cell. In this case, the Kapitza resistance,

$$R_K = \frac{1}{G} = \frac{\Delta T}{J_z}, \quad (3.6)$$

depends on the imposed kinetic energy flux, J_z , in a direction normal to the interface (z), and the steady-state temperature drop, ΔT , across the interface.[49]

3.3 Computational Details

Solvated gold nanoparticles ranging in diameter from 20-80 Å were simulated using reverse non-equilibrium molecular dynamics (RNEMD) in a spherical shell of hexane. Similar planar systems, displaying (111), (110), and (100) facets with hexane solvent were also prepared. The following sections describe the system composition, the potentials used to calculate the interactions in the system, as well as the simulation protocol.

3.3.1 System Composition

Both the nanoparticle and planar systems contain only gold atoms and hexane molecules. The composition of the planar systems can be found in Table 3.1 and the nanoparticle system details can be found in Tables 3.2, 3.3, and 3.4.

TABLE 3.1

Composition of the solvated planar facet systems and the physical extent of the gold slabs (L_x , L_y , and L_z). The hexane molecules occupy the remainder of a 100 Å box (length measured along the z -axis).

Facet	Au atoms	L_x (Å)	L_y (Å)	L_z (Å)	Hexane Molecules
(111)	972	25.915	29.888	18.952	284
(110)	1800	40.131	34.089	20.280	498
(100)	1008	24.322	24.382	26.422	200

TABLE 3.2

Composition of the solvated nanosphere simulations.

Particle Radius (Å)	Components	
	Au atoms	Hexane Molecules
9.20 ± 0.28	249	2894
14.30 ± 0.31	887	6304
19.07 ± 0.28	1985	8555
24.09 ± 0.32	3925	11576
29.03 ± 0.29	6699	15376
34.01 ± 0.32	10641	9235
38.88 ± 0.31	15707	8056

Planar systems were constructed with the exposed (hkl) facets directed normal to the positive and negative z -axis. The simulation cell dimensions were set by the facet, and the simulation box was enlarged along the z dimension to a fixed size of 100 Å. The remaining space was filled with hexane molecules to a density of 0.6548 g cm⁻³.

3.3.2 Force Fields

For this work, gold – gold interactions are calculated using the quantum Sutton-Chen (QSC) model.[90] The hexane solvent is described by the TraPPE united atom (UA) model.[2] The bonds in TraPPE-UA are rigid, but here the bonds are made flexible using harmonic force constants borrowed from OPLS-AA for intra-molecular sites closer than 3 bonds.[?] The interactions between Au atoms and atoms on the hexane molecules were fit to a pairwise Lennard-Jones potentials based on a study by Hautman and Klein for Au(111) surfaces.[7] Details of the interaction potentials are identical to previous work and previous chapter on heat transport for thiolate-protected gold nanospheres.[60]

3.3.3 Simulation Protocol

The gold nanospheres were prepared by cutting a FCC lattice with radii ranging 10 - 40 Å. Icosahedral particles were constructed in nested shell structures, built around an ideal icosahedral core. Cuboctahedral particles were built by cutting (111) and (100) facets from a FCC lattice. All particles were thermally equilibrated before being solvated with thermally equilibrated hexane using packmol.[96] Once solvated, the systems were equilibrated for a minimum of 1 ns using the Langevin Hull integrator with an external bath characterized by 50 atm of pressure and a temperature bath at 250K.[1] Random seeds were used in both the packing of the solvent and the equilibration process to ensure independent samples.

TABLE 3.3

Composition of the solvated icosahedral nanoparticle simulations.

<i>n</i> shells	radius (Å)	Components	
		Au atoms	Hexane Molecules
4	9.45 ± 0.15	309	2894
5	11.75 ± 0.17	561	4320
6	14.07 ± 0.19	923	6304
7	16.39 ± 0.21	1415	7414
8	18.71 ± 0.25	2057	8555
9	21.04 ± 0.27	2869	8555
10	23.36 ± 0.30	3871	11576
11	25.69 ± 0.32	5083	11576
12	28.02 ± 0.35	6525	11576
13	30.35 ± 0.38	8217	7741
14	32.67 ± 0.41	10178	9235
15	35.00 ± 0.43	12430	10911
16	37.33 ± 0.66	14993	11576

TABLE 3.4

Composition of the solvated cuboctahedral nanoparticle simulations.

radius(Å)	Components	
	Au atoms	Hexane Molecules
7.41 ± 0.35	147	11360
10.16 ± 0.53	309	3387
12.15 ± 0.50	561	5888
14.98 ± 0.69	923	7414
16.93 ± 0.65	1415	9440
19.80 ± 0.85	2057	9380
21.73 ± 0.82	2869	10317
24.13 ± 0.90	3871	14185
26.53 ± 0.99	5083	19585
31.34 ± 1.15	8217	12626
36.15 ± 1.32	12431	17457

Planar interfaces displaying the Au(111), Au(110), and Au(100) facets were prepared as slabs ~ 20 Å thick with the relevant facets rotated normal to the z -axis. Surface stress was removed by relaxing the systems for 1 ns at 250 K in a constant surface tension ($N\gamma T$) ensemble with zero applied surface tension, followed by 1 ns in the microcanonical (NVE) ensemble. Hexane molecules were packed into the remaining box volume with a density of 0.6548 g/cm³. The solvated systems were then equilibrated using the canonical (NVT) ensemble at 250 K for 1 ns followed by further relaxation in the microcanonical ensemble for 1 ns.

Following equilibration, the relevant thermal flux was applied for 1 ns for the nanoparticle systems and 3 ns for the planar systems, allowing for a steady-state temperature gradients to develop. Mean temperatures of the system remained at 250K, preserving the solvent cluster around the nanoparticles and preventing the formation of a vapor layer. Thermal coupling to the external temperature bath was removed to avoid interference with the imposed flux. The metal particles equilibrated rapidly, and were typically found with elevated temperatures (~ 300 K) relative to the bulk. Because the solvent volume is large relative to the particles, the solvent finds a steady state temperature just below 250K throughout most of the volume. Adjacent to the surface of the particles, solvent temperatures are typically close to 260K. The TraPPE-UA hexane model boils at ~ 330 K, so the simulation conditions are reasonable for maintaining liquid surroundings for the particles. All simulations were carried out with the open source molecular dynamics package, OpenMD.[94, 95]

Five separate configurations for each system size were simulated to provide statistical independence of the hexane packing. Thermal conductance was calculated using the same methods found in Stocker *et al.*[60] for the non-periodic systems and for the planar systems.[55]

3.4 Results and Discussion

The interfacial thermal conductance (G) for hexane-solvated spherical, icosahedral, and cuboctahedral Au nanoparticles was computed using RNEMD simulations, and was compared with the same quantity for a series of planar gold interfaces, including the Au(111), Au(100), and Au(110) interfaces. These surfaces are all exhibited as microfacets on the surfaces of the nanospheres, and the Au(111) facet is the primary facet displayed by the icosahedra, where the cuboctahedra display Au(111) and Au(100).

Computed interfacial thermal conductance values for the icosahedra, cuboctahedra, nanospheres, and flat facets are shown in Fig. 3.1. The nanospheres have a pronounced dependence on the particle radius, r , while the icosahedral conductance stays relatively close to the value obtained for the Au(110) facet. Thermal transport out of the cuboctahedral particles show a mostly linear dependence on particle radius. The smooth line going through the conductance values for the spheres is a fit using the Tascini *et al.*[61] model (Eq. (3.1)) with $G(\infty) = 49.25 \text{ MW m}^{-2} \text{ K}^{-1}$, and $\delta = -156.25 \text{ MW \AA m}^{-2} \text{ K}^{-1}$. Notably, our simulations project a value for the interfacial conductance of the infinite spheres that is significantly *higher* than many of the flat facets. To explain this observation, the surface density of undercoordinated atoms and the vibrational densities of states of these undercoordinated atoms are discussed in the following sections.

The spherical particles display all three of the planar facets (as well as small regions of higher index facets), and for most of the size range simulated, they also exhibit a significantly higher interfacial thermal conductance than the low-index facets.

For icosahedral particles, there is no clear dependence of G on the particle size, and the larger particles exhibit thermal conductance values slightly above the expected (111) conductance for particles with $r \approx 35 \text{ \AA}$. There is some instability in the values of G in the range of $r = 18 - 22 \text{ \AA}$, which is near the transition from stable icosahedra

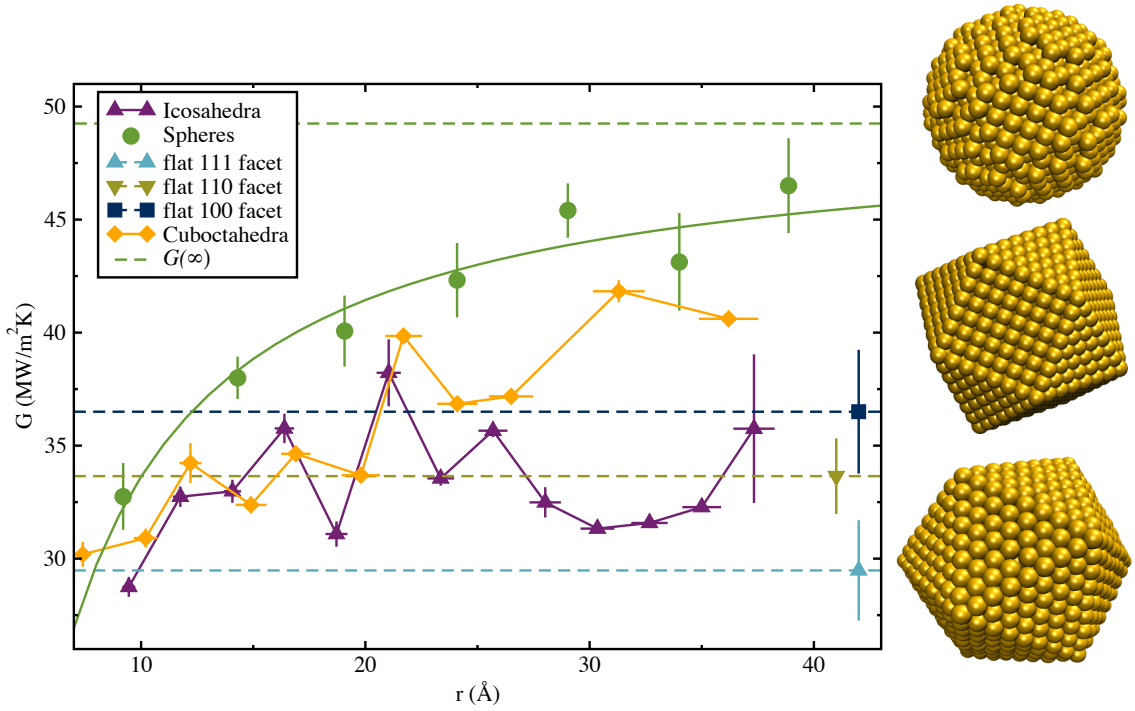


Figure 3.1. Interfacial thermal conductance, G , for bare gold nanospheres, cuboctahedra, and icosahedra in contact with hexane solvent.

Conductances for flat Au(111), Au(100), and Au(110) interfaces are indicated with dashed horizontal lines. A fit using the model of Tascini *et al.* is shown along with the predicted value of $G(\infty)$, the infinite particle limit.

to cuboctahedra.[?]

3.4.1 Hexane Density

The hexane density as function of distance from the gold at the interface of the planar facets is provided in Fig. 3.2. The solvent in the (111) and (100) systems display similar behavior, while the solvent near the (110) interface comes closer to the surface atoms. In the (110) system, the first layer of hexane is spread out over a thicker slab in comparison to the other two systems and allows solvent to come closer to the interfacial atoms. This is likely due to the ridges present on this interface. Within 5 Å of the interfacial gold layer, the three systems have the same amount of hexane.

3.4.2 Surface Atom Undercoordination

For the three flat facets, the primary feature that differentiates the facets is the coordination number (CN) of the atoms that are exposed to the solvent. In bulk Au, the coordination number of the atoms is twelve; six neighbors in plane, three below the atom, and three above the atom. Any atom with a coordination number below twelve would exhibit more vibrational freedom and is considered an undercoordinated site. The Au(111) surface presents gold atoms with nine surrounding metallic atoms ($CN = 9$) to the solvent, while the Au(100) facet surface exposes atoms with $CN = 8$. Au(110) displays a corrugated surface where the two outer layers of atoms have $CN = 7$ and $CN = 11$, respectively (displayed in 3.3). Both of the (110) surface atoms coordination environments approach the surface close enough to interact with the solvent atoms.

In Table 3.5, the surface density of undercoordinated atoms for a set of ideal geometries are provided. The population density for the sphere systems in the large

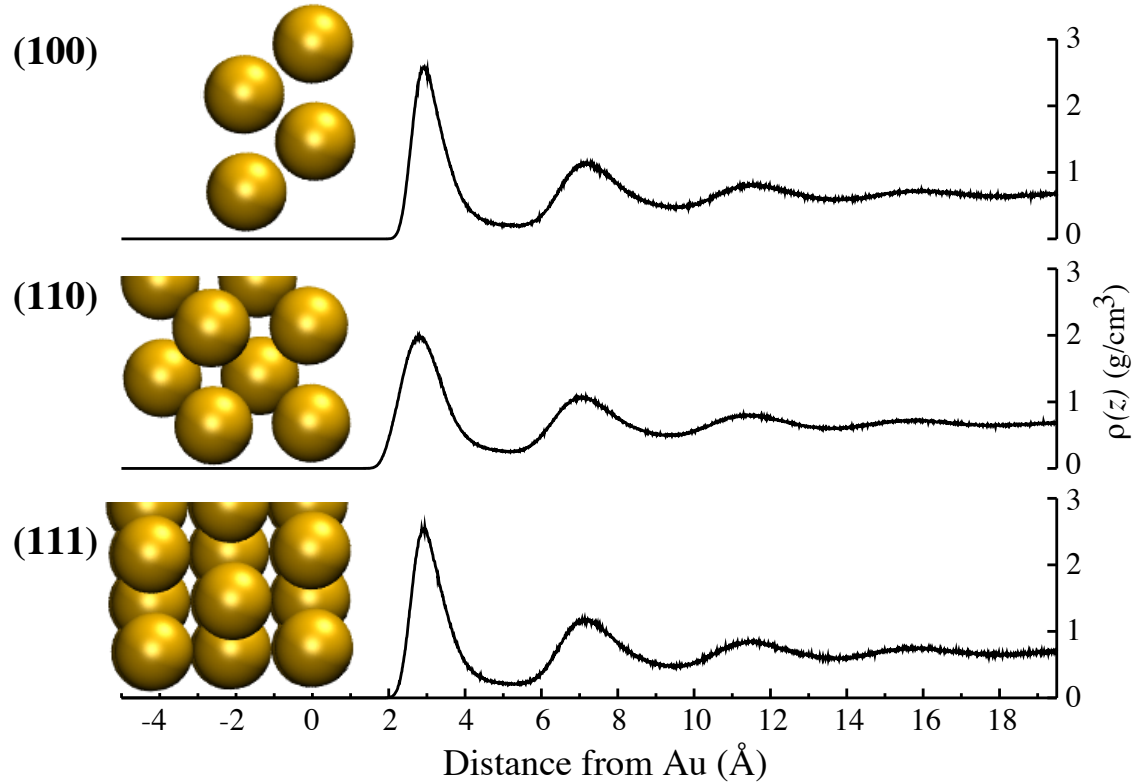


Figure 3.2. Hexane density as a function of distance from the interfacial gold for the (111), (110), and (100) facets. The solvent in the (111) and (100) systems display nearly identical density profiles. Because the lowest-coordinated gold atoms on the (110) facet have a relatively low surface density, the hexane molecules are able to get closer to these undercoordinated atoms.

TABLE 3.5

Surface densities (\AA^{-2}) of undercoordinated atoms in ideal geometries. ℓ (\AA) is the lattice constant of the underlying FCC lattice. The spheres and cuboctahedra are calculated using a gold FCC lattice with $\ell = 4.08 \text{ \AA}$. For cuboctahedral particles, the radius (r) is computed using Eq. (3.15).

surface	Coordination Number			
	6	7	8	9
(111)	0	0	0	$\frac{4\sqrt{3}}{3\ell^2}$
(100)	0	0	$\frac{2}{\ell^2}$	0
(110)	0	$\frac{\sqrt{2}}{\ell^2}$	0	0
Spheres (large r limit)	0.021	0.025	0.021	0.032
Icosahedra (n shells)	$\frac{8\sqrt{3}}{5\ell^2 n^2}$	0	$\frac{4\sqrt{3}(n-1)}{\ell^2 n^2}$	$\frac{4(n-1)}{\sqrt{3}\ell^2 n}$
Cuboctahedra	0	$\frac{1}{r\ell} \left(\frac{3\sqrt{2}+2\sqrt{6}}{3+\sqrt{3}} \right)$	$\frac{6}{(3+\sqrt{3})\ell^2}$	$\frac{4}{(3+\sqrt{3})\ell^2}$

radius limit are taken by averaging the surface densities for ideal gold nanospheres with radii of 95–100 Å. For other FCC-based nanoparticles, it is relatively simple to convert these surface densities using the lattice constant of gold, $\ell = 4.08$ Å.

Planar facets have a fixed population density based on the number of exposed undercoordinated atoms and the physical dimensions of the exposed facet area in terms of the lattice constant. In an ideal icosahedral nanoparticle with n shells, the surface population density is computed using the number of vertex, edge, and face atoms,

$$n_{\text{vertex}} = 12, \quad (3.7)$$

$$n_{\text{edge}} = 30(n - 1), \quad (3.8)$$

$$n_{\text{face}} = 10n^2 - 30n + 20. \quad (3.9)$$

The number of shells, n , is also directly related to the particle edge length (a), radius (r), and surface area (A) of the icosahedral particle,

$$a = \ell n \quad (3.10)$$

$$r = \frac{\ell n \sqrt{10 + 2\sqrt{5}}}{4} \quad (3.11)$$

$$A = \ell^2 n^2 5\sqrt{3} \quad (3.12)$$

where ℓ is the lattice constant.

For ideal cuboctahedra, the edge length (a) can be used to determine surface areas for the eight triangular (111) faces and six square (100) faces,

$$A_{(111)} = 2\sqrt{3}a^2 \quad (3.13)$$

$$A_{(100)} = 6a^2 \quad (3.14)$$

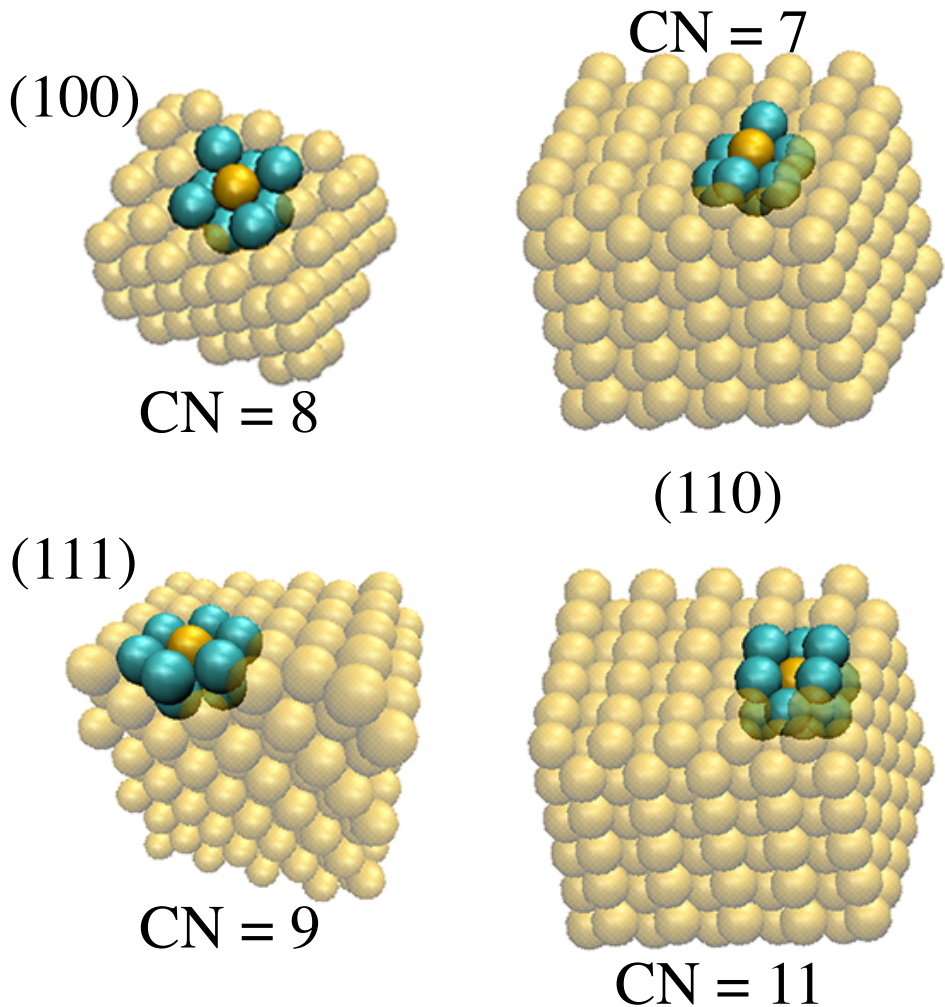


Figure 3.3. Locations of undercoordinated atoms on common gold facets. The dark gold atoms indicate atoms of a particular coordination number, cyan atoms denote the first nearest neighbors of these atoms, and the partially transparent lattice illustrates the location of the atoms in the larger gold structure. (111) surfaces (lower left) display atoms with CN=9, while (100) surfaces (upper left) display atoms with CN=8, and (110) surfaces present surface atoms with CN=7 and buried atoms with CN=11.

In addition, cuboctahedra have twenty-four edges ($CN = 7$, length = a), and twelve vertices ($CN = 5$). An approximate radius of the cuboctahedral particles can be found by averaging the diameter between parallel square faces and parallel triangular

faces,

$$r = \frac{a}{2} \left(\frac{\sqrt{2}}{2} + \frac{\sqrt{6}}{3} \right) \quad (3.15)$$

Table 3.5. Surface densities of the CN=9 and CN=8 sites are computed using the fraction of total surface area in each of the (111) and (100) facets, respectively. For small particles, the edge atoms (CN=7) can dominate, but for larger particles, the ratio of CN=8 and CN=9 atoms is constant.

Reducing the number of metallic interactions allows the surface atoms to vibrate at different frequencies than the interior atoms, populating a portion of the spectrum that overlaps with collective motions of the solvent molecules. This mechanism may explain the enhanced interfacial thermal conductance of the (100) facet relative to the (111) facet. However, it does not explain why the (110) facet displays an intermediate conductance even though the surface atoms have a lower coordination number than the (100) facet. To answer this question, it is important to consider the surface density of the undercoordinated atoms as well as the vibrational freedom allowed by the undercoordination. In Table 3.6 the density of the solvent-accessible undercoordinated surface atoms for the three facets is shown. Although the (110) facet displays 7- and 11-coordinated atoms to the solvent, the CN = 11 have vibrational dynamics that are essentially equivalent to the bulk gold (Fig. 3.4), and the surface density of these atoms is significantly lower than the surface density displayed by the (111) and (100) facets.

It is therefore likely that not only the undercoordination of surface atoms, but also the density of these undercoordinated atoms plays a role in thermal conductance. In the nanoparticles, surface atoms that are in physical contact with the solvent have a range of coordination numbers from 5 – 9, but only CN = 6 – 9 appear with high probability. The surface coordination densities have been calculated for all of our samples, and the undercoordination density is distinct for the spheres, icosahedra,

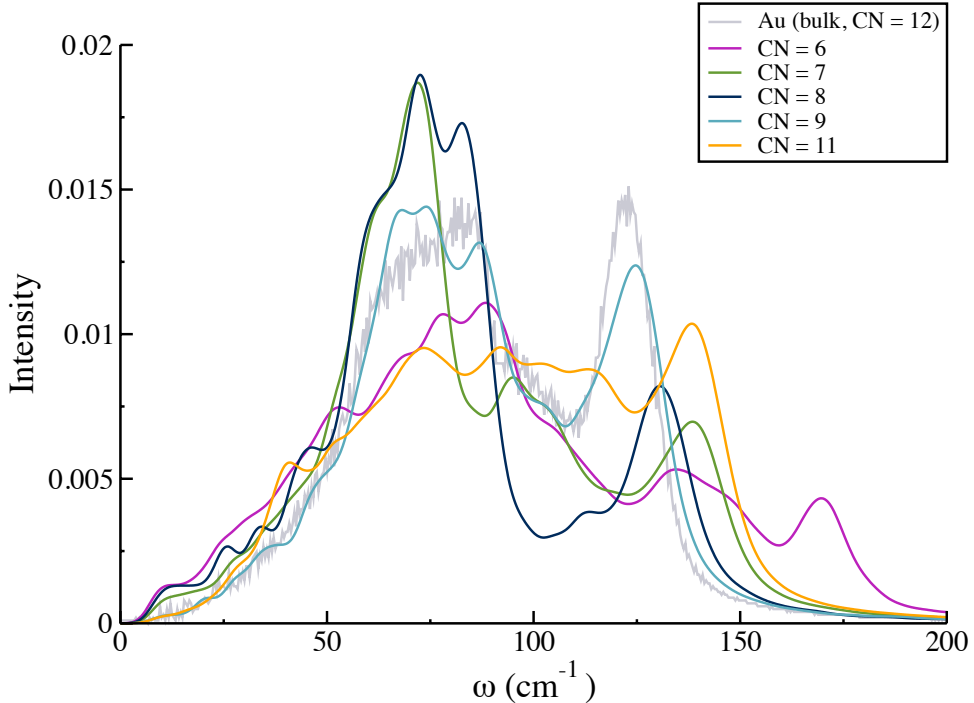


Figure 3.4. The normalized low frequency density of states (DOS) of the surface atoms with the coordination number of 6, 7, 8, 9 and 11, corresponding to the vertices of the icosahedra, Au(110), Au(100), Au(111) and subsurface Au(110), respectively. Note that CN=11 atoms near a surface are found adjacent to atoms with lower coordination (e.g. CN=7), so the high frequency peak at 138 cm^{-1} is present for both CN=11 and CN=7. Low frequency contributions at $\sim 70\text{ cm}^{-1}$ are enhanced for surface atoms with CN=7, 8, and 9.

and cuboctahedra (See Fig. 3.5).

The icosahedral particles display three coordination environments: the vertices have a CN = 6, while the triangular (111) faces of the particle have a CN = 9, and the edges connecting the faces have CN = 8. As the radius of the icosahedral particles increases, the surface is dominated by the triangular facets, so the surface density of the CN = 9 rises. For perfect icosahedra, the ideal surface densities are shown as dashed lines in Fig. 3.5.

For the simulated systems at 250K, surface vibrational motion leads to coordina-

TABLE 3.6

The density of undercoordinated gold atoms at the surface of a facet.

Facet	CN	Surface Density (atoms Å ⁻²)
(111)	9	0.1394
(100)	8	0.1214
(110)	7	0.0877
	11	0.0877

tion numbers that are lower than one would expect for an ideal icosahedron. This is evident in the populations of the CN = 9, which is 20-50% lower than the ideal case.

In the spherical particles, the surface density of undercoordinated atoms stabilizes above $r = 25$ Å. However, the densities of the undercoordinated atoms never approach any of the flat facet values (as is the case in the icosahedra). We may estimate the large radius limit of the spheres by averaging the surface densities for ideal spheres of radii 95–100 Å. These are shown with open symbols in the upper panel of Fig. 3.5.

The cuboctahedral particles approach the ideal solid surface densities as the radius of the particle increases. Beyond a radius of 15 Å the cuboctahedra are no longer dominated by edge atoms and flat facets form the majority of the surface. After this transition the surface densities quickly stabilize to nearly-ideal cuboctahedral structures.

3.4.3 Phonon Spectra

By selecting specific groups of atoms while computing the vibrational power spectrum (Eq. 3.4) the role of undercoordination on surface vibrational motion can be

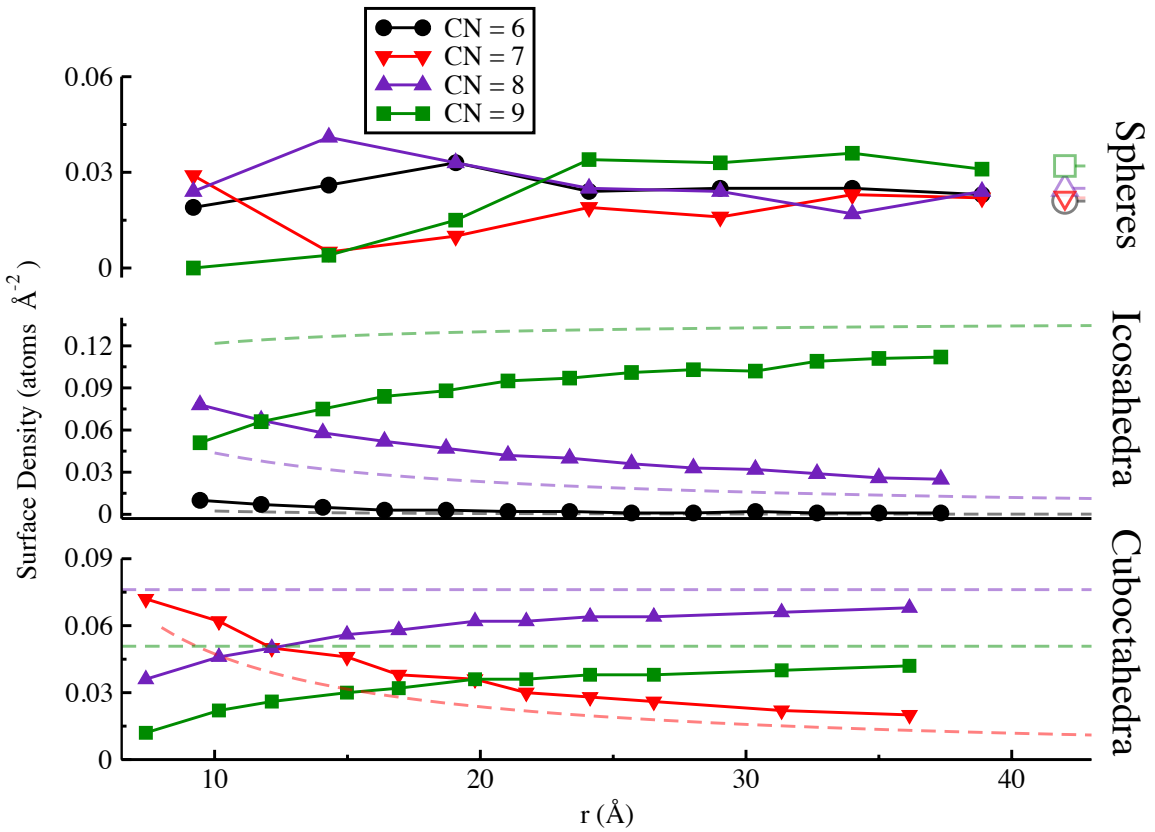


Figure 3.5. The coordination number of surface atoms as a function of particle size. Filled data points are sampled from simulations, while the dashed lines correspond to ideal icosahedral and cuboctahedral solids. In the spherical case, the large radius limits are shown with open symbols. The large radius limit for the spheres approaches a constant density for all undercoordinated sites, while for the icosahedra, the 9-coordinated (111) facet dominates. In larger cuboctahedra, the relative fraction of 8- and 9-coordinated surface atoms is largely independent of particle size.

explored. For thermal transport, the regions of interest are the nanoparticle atoms in direct physical contact with the solvent, and those solvent molecules that form the first solvation shell, i.e. $< 5\text{\AA}$ from the gold surface.

Under the QSC potential, the bulk gold vibrational power spectrum displays two broad peaks, one at $\sim 60\text{--}80 \text{ cm}^{-1}$, and another sharper peak at $\sim 125 \text{ cm}^{-1}$. The vibrational densities of states for the four outer layers of the nanoparticles are shown in Fig. 3.7. The surface layers for all particles are dominated by the low frequency portion of the spectrum ($< 70 \text{ cm}^{-1}$) and display small morphology-dependent features at higher frequencies (140 cm^{-1}). The low-frequency peak appears at significantly lower frequencies than in the bulk, and the higher frequency contribution is significantly broadened. Spheres and cuboctahedra recover bulk-like densities of states relatively close to the surface – only the surface and second shell are significantly altered from the bulk gold density of states. In the spheres, the higher frequency contribution ($\sim 150 \text{ cm}^{-1}$) resembles the vibrational density of states for undercoordinated atoms with CN=8 or 7 (see Fig. 3.4).

3.4.4 A Brief Aside

The icosahedra still have perturbed spectra even four layers into the particles. Icosahedral particles grow around a core with I_h symmetry, and the local environment around the atoms deviates significantly from perfect FCC ordering. The local bond orientational order can be described using the method of Steinhardt *et al.*[97] The local bonding environment, $\bar{q}_{\ell m}$, for each atom in the system is determined by averaging over the spherical harmonics between that atom and each of its neighbors,

$$\bar{q}_{\ell m} = \sum_i Y_{\ell}^m(\theta_i, \phi_i) \quad (3.16)$$

where θ_i and ϕ_i are the relative angular coordinates of neighbor i in the laboratory frame. A global average orientational bond order parameter, $\bar{Q}_{\ell m}$, is the average over each $\bar{q}_{\ell m}$ for all atoms in the system. To remove the dependence on the laboratory coordinate frame, the third order rotationally invariant combination of $\bar{Q}_{\ell m}$, \hat{w}_ℓ , is utilized here.[97, 98]

For $\ell = 4$, the ideal face-centered cubic (FCC) local structures exhibit \hat{w}_4 values near -0.159. Because \hat{w}_4 exhibits an extreme value for fcc structures, it is ideal for measuring local FCC ordering. The spatial distribution of \hat{w}_4 local bond orientational order parameters, $p(\hat{w}_4, r)$, can provide information about the location of individual atoms that are central to local FCC ordering.

The fraction of FCC-ordered gold atoms at a given radius in the nanoparticle,

$$f_{\text{fcc}}(r) = \int_{-\infty}^{w_c} p(\hat{w}_4, r) d\hat{w}_4 \quad (3.17)$$

is described by the distribution of the local bond orientational order parameters, $p(\hat{w}_4, r)$, and w_c , a cutoff for the peak \hat{w}_4 value displayed by fcc structures. As in our previous work,[60] w_c value of -0.12 was chosen to isolate the fcc peak in \hat{w}_4 .

As shown in Fig. 3.6, the FCC ordering persists in the spheres even quite close to the surface, while the icosahedra have significant populations that deviate from FCC local ordering. The cuboctahedra do not have uniform gold population between 30 and 40 Å, so the fraction of FCC ordering decays starting at 30 Å. Although I cannot conclude that this is the cause of the differences in the VDOS for the icosahedral particles, it is likely that local ordering in the metal can alter the bulk densities of states.

Comparison of the vibrational density of states of all the gold atoms displays some important differences between the icosahedral structures and the FCC-based spheres and cuboctahedra (Fig. 3.8). Icosahedral particles have non-FCC ordering

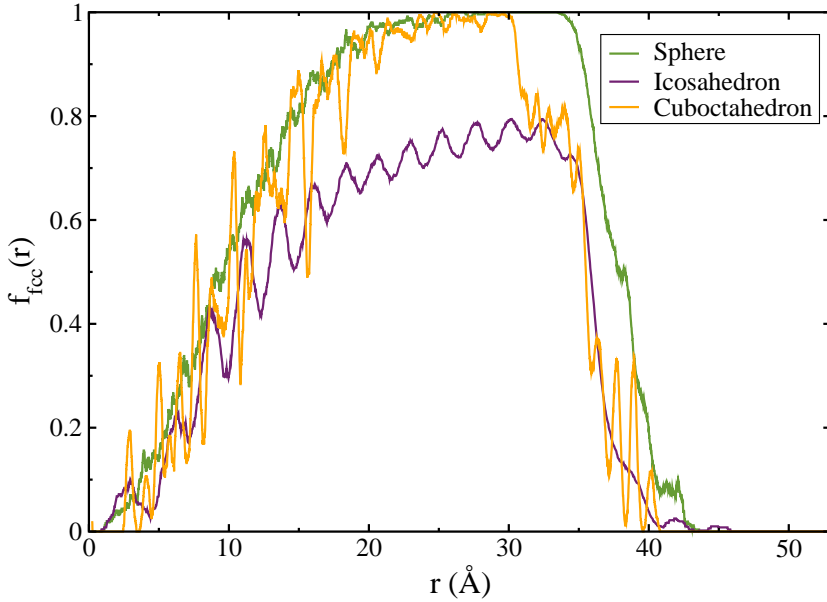


Figure 3.6. The fraction of FCC-like local environments as a function of radius from the center of 40 Å nanoparticles. The spheres and cuboctahedra are originally cut from a FCC lattice, so the local ordering persists even close to the surface. Icosahedra are constructed as shells surrounding a perfectly icosahedral central core of 13 atoms. Non-FCC ordering persists throughout these simulations.

deep into the particle, and this manifests as a shift in phonon population from the broad low-frequency region to the higher frequency peak, even for the largest of the particles that were studied. For comparison, the largest spheres and icosahedra have only slight differences in their “bulk” phonon density of states.

At the surfaces of the particles, the differences are nearly all in the higher frequency portion of the spectrum ($> 100\text{cm}^{-1}$), indicating that the surface undercoordination primarily alters high-frequency transmission into the solvent. This suggests roles for bulk crystalline ordering as well as surface undercoordination in any model for the interfacial thermal conductance.

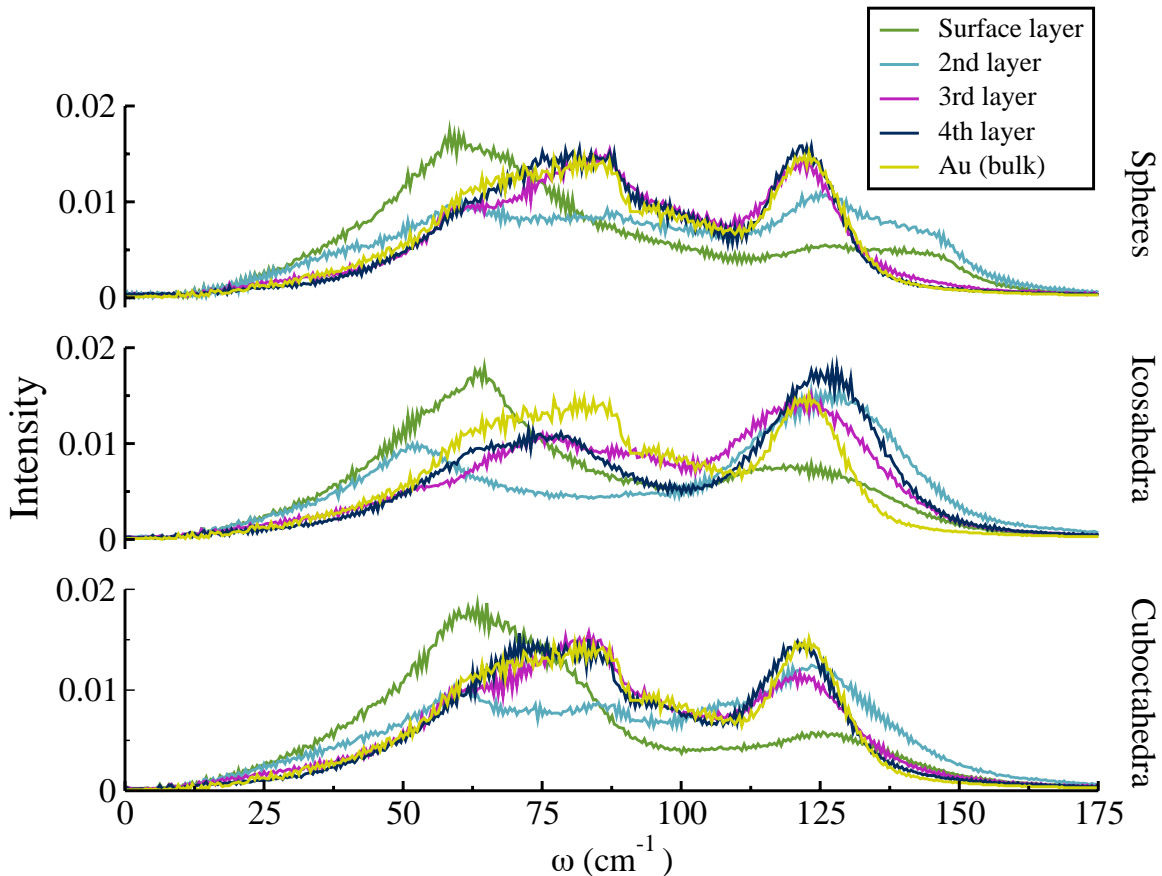


Figure 3.7. The projected vibrational density of states (Eq. 3.4) for individual layers in the largest gold nanoparticles (top: spheres, middle: icosahedra, bottom: cuboctahedra). In all systems, the surface layer (green) is significantly enhanced at low frequencies and is shifted down by $\sim 20 \text{ cm}^{-1}$. The Au (bulk) curve shown for comparison is from a perfect FCC lattice in periodic boundary conditions.

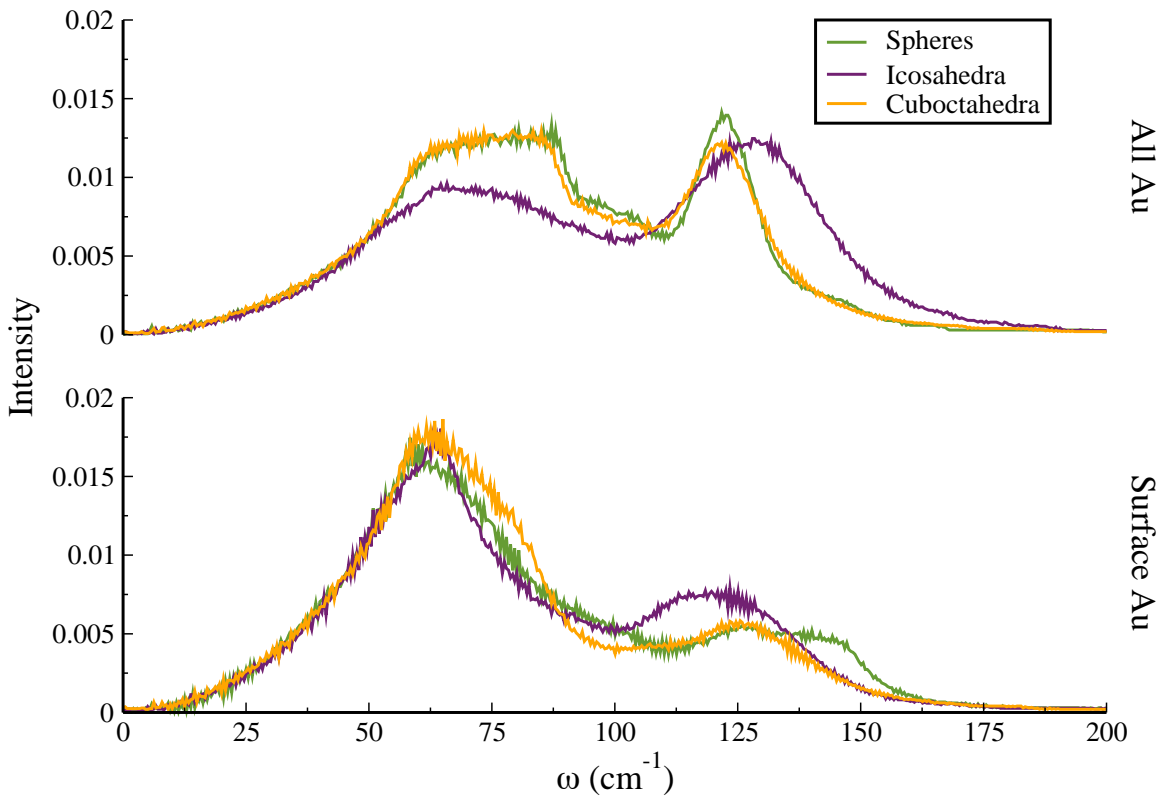


Figure 3.8. The projected vibrational density of states for all gold atoms (top panel) shows that the phonons in FCC-like nanoparticles (spheres, cuboctahedra) have similar frequency representation, while the non-FCC structures (icosahedra) have significantly altered “bulk” spectra. For surface atoms (bottom panel), the differences in surface undercoordination appear at higher frequencies. These spectra were computed for the largest particles in each of the different morphologies.

Except in the case of the icosahedra, vibrational power spectra that include all gold atoms in the nanoparticles do not show significant dependence on particle radius (see Fig. 3.9). This suggests that mismatch models (like AMM or DMM) that use only bulk properties will not be able to capture the surface behavior that is relevant to heat transfer at the nanoscale.

Solvent vibrational densities of states are remarkably similar for the icosahedral and spherical particles, even for solvent that is within 5 Å of the interface (Fig. 3.9). While the solvent VDOS in the icosahedral and spherical systems shows only small changes as a function of particle size, the solvent in the cuboctahedral systems appears to shift to lower frequencies with increasing particle radius. The gold VDOS in all systems displays a shift from the low frequency peak, 70 cm^{-1} , to a peak at 125 cm^{-1} as the particle radii increases and there is a significant difference between the two FCC structures and the icosahedra spectra. The FCC structures increase in intensity at 125 cm^{-1} with increasing particle radius, while the icosahedra VDOS shows a shift in population from low frequencies to the higher frequency peak. Note that the gold shown in Fig. 3.9 includes all layers of the particles.

Due to the similarity in solvent VDOS, a model for interfacial thermal transport in these systems would need to include the lattice structure of the particle and the quantity and solvent accessibility of specific kinds of undercoordinated metal atoms.

3.4.5 A Simple Model for Bare Nanoparticle Conductance

The vibrational densities of states suggest the bare metallic nanoparticles exhibit different bulk phonon frequencies that depend on crystalline packing, and different surface spectra that depend on surface undercoordination. Both of the bulk and surface frequencies can effect thermal transport, so a simple model in terms of a

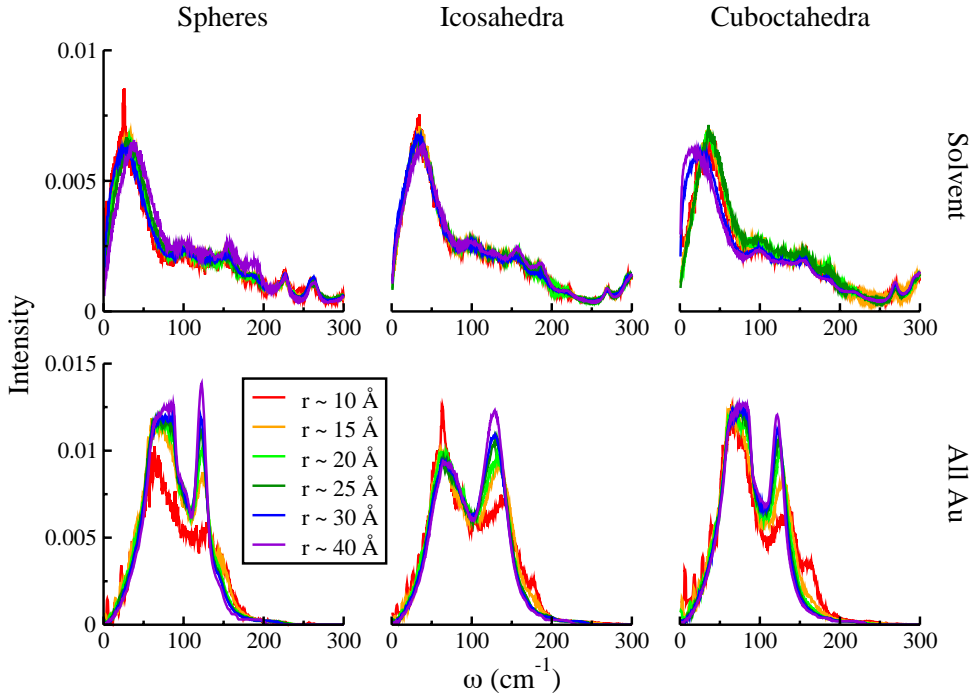


Figure 3.9. The normalized low frequency density of states (DOS) of the interfacial solvent and the gold particle for the icosahedral and spherical systems.

linear combination of surface densities of undercoordinated atoms can be explored,

$$G \approx a \text{ CN}_6 + b \text{ CN}_7 + c (1 + c' \delta_{\text{ico}}) \text{ CN}_8 + d (1 + d' \delta_{\text{ico}}) \text{ CN}_9 \quad (3.18)$$

where, $a-d$ are coordination transport coefficients with the units of 10^{-20} MW/K and CN_n have surface density units ($1/\text{\AA}^2$) for surface atoms with coordination number n . The delta function, δ_{ico} is set to unity for icosahedral structures, and zero for FCC-like nanoparticles. The coefficients c' and d' are weighting factors that recognize the differences in the bulk density of states in the icosahedral particles. Fitting the six parameters was done using a simple ordinary least squares model with data from all simulated particles.

TABLE 3.7

Parameters of the Model in Eq. (3.18).

a	b	c	c'	d	d'
858.9405	183.9062	291.7960	-0.5943	369.6250	-0.2498

With Eq. (3.18) it should be possible to predict the interfacial thermal conductance for bare gold nanoparticles in hexane based only on a structural analysis of the surface for coordination densities and the interior of the particle for crystalline structure. The predicted (and simulated) values of the thermal conductance are given in Fig. 3.10. With a coefficient of determination (R^2) value of 0.656, this fit does not predict G with a high degree of certainty, but it does suggest the large role that undercoordinated surface atoms play in conductance. Coefficients used in Eq. (3.18) are given in Table 3.7.

The coefficients provide some information about the thermal transport capabilities of each type of undercoordinated surface atom. These fits suggest that severely undercoordinated atoms (CN=6) transfer the largest amount of heat per atom, although their population in all systems is low.

It is also important to note that this fit considers the two different types of particles when finding the best fits for the most populous surface atoms (CN=8, CN=9). If the system is FCC-like the weight of the CN = 8 and CN = 9 are 2.464 and 1.333 times larger than their contributions from icosahedral cores.

Since the coefficients are related to the amount of energy transferred per atom type, these atoms on the FCC-like structures transfer a larger amount than in the icosahedral structure. This is likely due to differences in the underlying “bulk” densities of states.

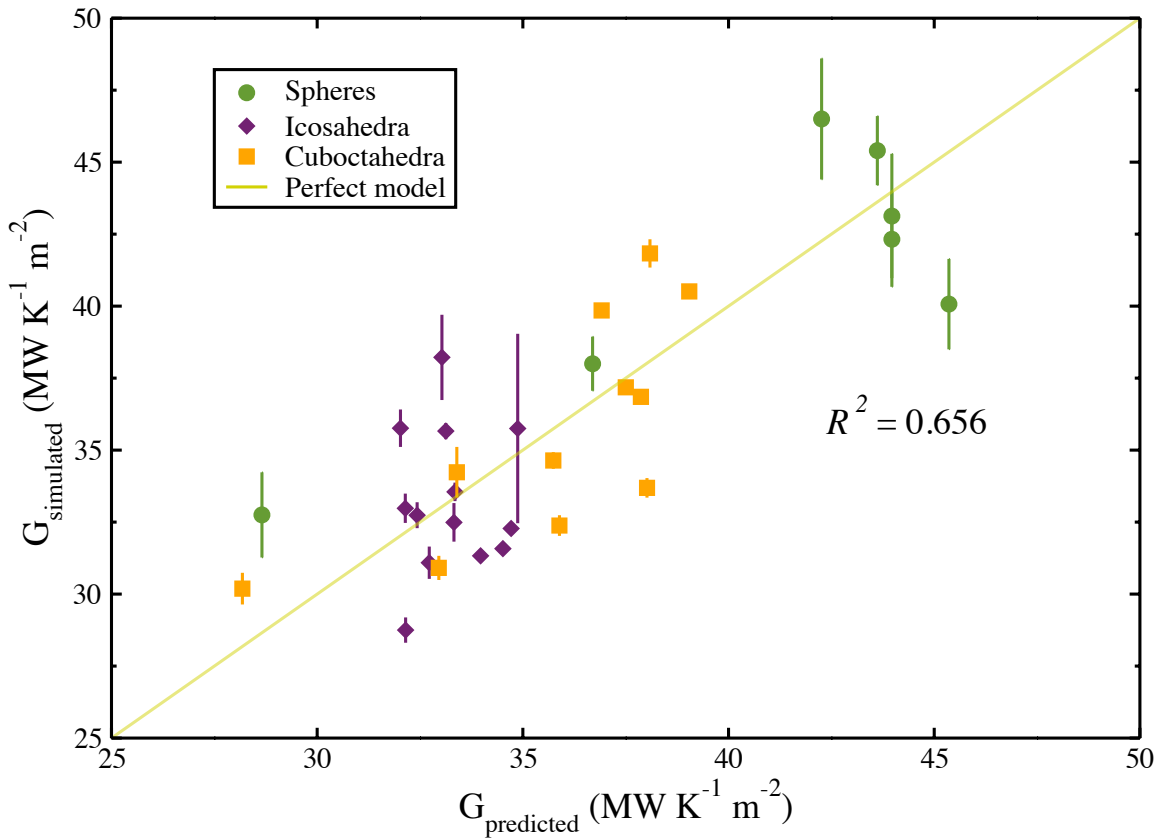


Figure 3.10. Structurally-predicted thermal conductance values from Eq. (3.18) compared with the simulated thermal conductance values. Error bars indicate the standard error computed using five replica simulations.

3.5 Conclusions

The primary observation of this work is that particle morphology has a significant effect on interfacial thermal conductance from bare particles to the surrounding solvent. In particular, spherical and cuboctahedra particles have a size-dependent interfacial thermal conductance, while icosahedral particles conduct heat to the surrounding solvent only slightly better than the flat (111) facets.

This work explored one explanation for this difference in terms of the density of undercoordinated sites on the surfaces of these three particle morphologies. Nanospheres, because they are carved out of an underlying FCC lattice, expose significantly undercoordinated atoms ($CN = 6 - 8$) to the solvent. For very small spheres, microfacets of (111), (100), and (110) dominate the surface, but for larger particles, the density of undercoordinated atoms becomes a significant fraction of the exposed atoms. In large icosahedral particles, the particles are dominated by (111) faces, and the $CN = 9$ atoms dominate the surface. Similarly, in large cuboctahedral particles, the (111) and (100) facets are both present, and the $CN = 9$ and $CN = 8$ atoms share the particle surface in a 2:3 ratio. Surface atom undercoordination leads directly to changes in the surface vibrational density of states, particularly at frequencies around $\sim 150\text{ cm}^{-1}$. The linear model suggests that differences in surface atom undercoordination (particularly for atoms that are undercoordinated relative to a flat facet) may be largely responsible for our observations.

This is not a complete explanation for the conductance values, however, as the large icosahedral particles exhibit G values above the planar (111) facet, and large cuboctahedra have G values above *both* the (111) and (100) facets. Edge and vertex atoms in these clusters may play an outsized role, and collective low-frequency modes of the particles may also be important, as the underlying “bulk” density of states also depends on particle morphology.

BIBLIOGRAPHY

1. Vardeman, C. F.; Stocker, K. M.; Gezelter, J. D. *J. Chem. Theory Comput.* **2011**, *7*, 834–842.
2. Martin, M. G.; Siepmann, J. I. *J. Phys. Chem. B* **1998**, *102*, 2569–2577.
3. Wick, C. D.; Martin, M. G.; Siepmann, J. I. *J. Phys. Chem. B* **2000**, *104*, 8008–8016.
4. Lubna, N.; Kamath, G.; Potoff, J. J.; Rai, N.; Siepmann, J. I. *J. Phys. Chem. B* **2005**, *109*, 24100–24107.
5. Luedtke, W. D.; Landman, U. *J. Phys. Chem. B* **1998**, *102*, 6566–6572.
6. Schapotschnikow, P.; Pool, R.; Vlugt, T. J. *Comput. Phys. Commun.* **2007**, *177*, 154 – 157.
7. Hautman, J.; Klein, M. L. *J. Chem. Phys.* **1989**, *91*, 4994–5001.
8. Chen, G. *Nanoscale Energy Transport and Conversion*; Oxford University Press: New York, 2005.
9. Goldstein, H.; Poole, C.; Safko, J. *Classical Mechanics*, 3rd ed.; Addison Wesley: San Francisco, 2001.
10. Kittel, C. *Introduction to Solid State Physics*; John Wiley and Sons: New York, 2005.
11. Hsieh, W.-P.; Lyons, A. S.; Pop, E.; Kebinski, P.; Cahill, D. G. *Phys. Rev. B* **2011**, *84*, 184107.
12. Stoner, R. J.; Maris, H. J. *Phys. Rev. B* **1993**, *48*, 16373–16387.
13. Monachon, C.; Weber, L.; Dames, C. *Annu. Rev. Mater. Res.* **2016**, *8*, 1–31.
14. Little, W. A. *Can. J. Phys.* **1959**, *37*, 334–349.
15. Graff, K. F. *Wave Motion in Elastic Solids*; Dover: New York, 1975.
16. Prasher, P. E., Ravi S. Phelan *J. Heat Transfer* **2000**, *123*, 105–112.
17. Prasher, R. *Applied Physics Letters* **2009**, *94*, 041905.

18. Lyeo, H.-K.; Cahill, D. G. *Phys. Rev. B* **2006**, *73*, 144301.
19. Swartz, E. T.; Pohl, R. O. *Rev. Mod. Phys.* **1989**, *61*, 605–668.
20. Reddy, P.; Castelino, K.; Majumdar, A. *Appl. Phys. Lett.* **2005**, *87*, –.
21. Beechem, T.; Graham, S.; Hopkins, P.; Norris, P. *Applied Physics Letters* **2007**, *90*, 054104.
22. Hopkins, P. E.; Duda, J. C.; Petz, C. W.; Floro, J. A. *Phys. Rev. B* **2011**, *84*, 035438.
23. Hopkins, P. E.; Duda, J. C.; Norris, P. M. *J. Heat Transfer* **2011**, *133*, 062401.
24. Stevens, A. N. N. P. M., Robert J. Smith *J. Heat Transfer* **2005**, *127*, 315–322.
25. Leach, A. *Molecular Modeling: Principles and Applications*, 2nd ed.; Pearson Educated Limited: Harlow, England, 2001.
26. Kohanoff, J.; Caro, A.; Finnis, M. *ChemPhysChem* **2005**, *6*, 1848–1852.
27. Baltazar, S. E.; Romero, A. H.; Rodriguez-Lopez, J. L.; Terrones, H.; Martonak, R. *Comp. Mat. Sci.* **2006**, *37*, 526–536.
28. Heyes, D. M. *Phys. Rev. B* **1988**, *37*, 5677–5696.
29. Massobrio, C.; Ciccotti, G. *Phys. Rev. A* **1984**, *30*, 3191–3197.
30. Helfand, E. *Phys. Rev.* **1960**, *119*, 1–9.
31. Viscardy, S.; Servantie, J.; Gaspard, P. *J. Chem. Phys.* **2007**, *126*, 184513.
32. Che, J.; Cagin, T.; Deng, W.; III, W. A. G. *J. Chem. Phys.* **2000**, *113*, 6888–6900.
33. Kinaci, A.; Haskins, J. B.; Çağın, T. *J. Chem. Phys.* **2012**, *137*, 014106.
34. Backer, J. A.; Lowe, C. P.; Hoefsloot, H. C. J.; Iedema, P. D. *J. Chem. Phys.* **2005**, *122*, 154503.
35. Hess, B. *J. Chem. Phys.* **2002**, *116*, 209–217.
36. Picalek, J.; Kolafa, J. *Mol. Simul.* **2009**, *35*, 685–690.
37. Vasquez, V. R.; Macedo, E. A.; Zabaloy, M. S. *Int. J. Thermophys.* **2004**, *25*, 1799–1818.
38. Evans, D. J. *Phys. Lett. A* **1982**, *91*, 457–460.
39. Erpenbeck, J. J. *Phys. Rev. Lett.* **1984**, *52*, 1333–1335.
40. Evans, D. J. *Phys. Rev. A* **1986**, *34*, 1449–1453.

41. Vogelsang, R.; Hoheisel, G.; Luckas, M. *Mol. Phys.* **1988**, *64*, 1203–1213.
42. Maginn, E. J.; Bell, A. T.; Theodorou, D. N. *J. Phys. Chem.* **1993**, *97*, 4173–4181.
43. Schelling, P. K.; Phillpot, S. R.; Keblinski, P. *Phys. Rev. B* **2002**, *65*, 144306.
44. Berthier, L.; Barrat, J. L. *J. Chem. Phys.* **2002**, *116*, 6228–6242.
45. Evans, D. J.; Searles, D. J. *Adv. Phys.* **2002**, *51*, 1529–1585.
46. Jiang, H.; Myshakin, E. M.; Jordan, K. D.; Warzinski, R. P. *J. Phys. Chem. B* **2008**, *112*, 10207–10216.
47. Müller-Plathe, F. *J. Chem. Phys.* **1997**, *106*, 6082–6085.
48. Müller-Plathe, F. *Phys. Rev. E* **1999**, *59*, 4894–4898.
49. Kuang, S.; Gezelter, J. D. *Mol. Phys.* **2012**, *110*, 691–701.
50. Zhang, M.; Lussetti, E.; de Souza, L. E. S.; Müller-Plathe, F. *J. Phys. Chem. B* **2005**, *109*, 15060–15067.
51. Tenney, C. M.; Maginn, E. J. *J. Chem. Phys.* **2010**, *132*, 014103.
52. Patel, H. A.; Garde, S.; Keblinski, P. *Nano Lett.* **2005**, *5*, 2225–2231.
53. Shenogina, N.; Godawat, R.; Keblinski, P.; Garde, S. *Phys. Rev. Lett.* **2009**, *102*, 156101.
54. Kuang, S.; Gezelter, J. D. *J. Phys. Chem. C* **2011**, *115*, 22475–22483.
55. Stocker, K. M.; Gezelter, J. D. *J. Phys. Chem. C* **2013**, *117*, 7605–7612.
56. Stocker, K. M.; Gezelter, J. D. *J. Chem. Theory Comput.* **2014**, *10*, 1878–1886.
57. Zanjani, M. B.; Lukes, J. R. *Journal of Applied Physics* **2014**, *115*.
58. Liu, M.; Ma, Y.; Wang, R. Y. *ACS Nano* **2015**, *9*, 12079–12087.
59. Wilhelmsen, Ø.; Trinh, T. T.; Kjelstrup, S.; Erp, T. S. V.; Bedeaux, D. *Phys. Rev. Lett.* **2015**, *114*, 065901.
60. Stocker, K. M.; Neidhart, S. M.; Gezelter, J. D. *J. Appl. Phys.* **2016**, *119*, 025106.
61. Tascini, A. S.; Armstrong, J.; Chiavazzo, E.; Fasano, M.; Asinari, P.; Bresme, F. *Phys. Chem. Chem. Phys.* **2017**, *19*, 3244–3253.
62. Wilson, O.; Hu, X.; Cahill, D.; Braun, P. *Phys. Rev. B* **2002**, *66*, 224301.

63. Ong, W.-L.; Rupich, S. M.; Talapin, D. V.; McGaughey, A. J. H.; Malen, J. A. *Nat Mater* **2013**, *12*, 410–415.
64. Kuang, S.; Gezelter, J. D. *J. Phys. Chem. C* **2011**, *115*, 22475–22483.
65. Ong, W.-L.; Majumdar, S.; Malen, J. A.; McGaughey, A. J. H. *J. Phys. Chem. C* **2014**, *118*, 7288–7295.
66. Hannah, D. C.; Gezelter, J. D.; Schaller, R. D.; Schatz, G. C. *ACS Nano* **2015**, *9*, 6278–6287.
67. Park, J.; Cahill, D. G. *Journal of Physical Chemistry C* **2016**, *120*, 2814–2821.
68. Pandey, H. D.; Leitner, D. M. *The Journal of Chemical Physics* **2017**, *147*, 084701.
69. Park, J.; Huang, J.; Wang, W.; Murphy, C. J.; Cahill, D. G. *J. Phys. Chem. C* **2012**, *116*, 26335–26341.
70. Ge, Z.; Cahill, D. G.; Braun, P. *Physical Review Letters* **2006**, *96*, 186101.
71. Neidhart, S. M.; Gezelter, J. D. *J. Phys. Chem. C* **122**.
72. Ge, Z.; Cahill, D. G.; Braun, P. V. *J. Phys. Chem. B* **2004**, *108*, 18870–18875.
73. Wang, Z.; Carter, J. A.; Lagutchev, A.; Koh, Y. K.; Seong, N.-H.; Cahill, D. G.; Dlott, D. D. *Science* **2007**, *317*, 787–790.
74. Schmidt, A. J.; Alper, J. D.; Chiesa, M.; Chen, G.; Das, S. K.; Hamad-Schifferli, K. *J. Phys. Chem. C* **2008**, *112*, 13320–13323.
75. Juvé, V.; Scardamaglia, M.; Maioli, P.; Crut, A.; Merabia, S.; Joly, L.; Del Fatti, N.; Vallée, F. *Phys. Rev. B* **2009**, *80*, 195406.
76. Alper, J.; Hamad-Schifferli, K. *Langmuir* **2010**, *26*, 3786–3789.
77. Harikrishna, H.; Ducker, W. A.; Huxtable, S. T. *Appl. Phys. Lett.* **2013**, *102*, –.
78. Cahill, D. G.; Ford, W. K.; Goodson, K. E.; Mahan, G. D.; Majumdar, A.; Maris, H. J.; Merlin, R.; Phillpot, S. R. *J. Appl. Phys.* **2003**, *93*, 793–818.
79. Losego, M. D.; Grady, M. E.; Sottos, N. R.; Cahill, D. G.; Braun, P. V. *Nat Mater* **2012**, *11*, 502–506.
80. Soussi, J.; Volz, S.; Palpant, B.; Chalopin, Y. *Appl. Phys. Lett.* **2015**, *106*.
81. Ge, Z.; Cahill, D. G.; Braun, P. V. *Phys. Rev. Lett.* **2006**, *96*, 186101.
82. Kikugawa, G.; Ohara, T.; Kawaguchi, T.; Torigoe, E.; Hagiwara, Y.; Matsumoto, Y. *J. Chem. Phys.* **2009**, *130*, –.

83. Tian, Z.; Marconnet, A.; Chen, G. *Appl. Phys. Lett.* **2015**, *106*, –.
84. Henz, B. J.; Hawa, T.; Zachariah, M. R. *Langmuir* **2008**, *24*, 773–783.
85. Badia, A.; Singh, S.; Demers, L.; Cuccia, L.; Brown, G. R.; Lennox, R. B. *Chem. Eur. J.* **1996**, *2*, 359–363.
86. Badia, A.; Gao, W.; Singh, S.; Demers, L.; Cuccia, L.; Reven, L. *Langmuir* **1996**, *12*, 1262–1269.
87. Badia, A.; Demers, L.; Dickinson, L.; Morin, F. G.; Lennox, R. B.; Reven, L. *J. Am. Chem. Soc.* **1997**, *119*, 11104–11105.
88. Badia, A.; Cuccia, L.; Demers, L.; Morin, F.; Lennox, R. B. *J. Am. Chem. Soc.* **1997**, *119*, 2682–2692.
89. Badia, A.; Lennox, R. B.; Reven, L. *Acc. Chem. Res.* **2000**, *33*, 475–481.
90. Qi, Y.; Çağın, T.; Kimura, Y.; Goddard III, W. A. *Phys. Rev. B* **1999**, *59*, 3527–3533.
91. Jorgensen, W. L.; Maxwell, D. S.; ; Tirado-Rives, J. *J. Am. Chem. Soc.* **1996**, *118*, 11225–11236.
92. Becke, A. D. *J. Chem. Phys.* **1993**, *98*, 5648–5652.
93. Lee, C.; Yang, W.; Parr, R. G. *Phys. Rev. B* **1988**, *37*, 785–789.
94. Gezelter, J. D.; Kuang, S.; Marr, J.; Stocker, K.; Li, C.; Vardeman, C. F.; Lin, T.; Fennell, C. J.; Sun, X.; Daily, K.; Zheng, Y.; Meineke, M. A. *OpenMD*; An open source molecular dynamics engine, version 2.1, <http://openmd.org> (accessed 11/13/2013).
95. Meineke, M. A.; Vardeman, C. F.; Lin, T.; Fennell, C. J.; Gezelter, J. D. *J. Comp. Chem.* **2005**, *26*, 252–271.
96. Martínez, L.; Andrade, R.; Birgin, E. G.; Martínez, J. M. *J. Comput. Chem.* **2009**, *30*, 2157–2164.
97. Steinhardt, P. J.; Nelson, D. R.; Ronchetti, M. *Phys. Rev. B* **1983**, *28*, 784–804.
98. Vardeman, C. F.; Gezelter, J. D. *J. Phys. Chem. C* **2008**, *112*, 3283–3293.
99. Segal, D.; Nitzan, A.; Hänggi, P. *J. Chem. Phys.* **2003**, *119*, 6840–6855.
100. Young, D. A.; Maris, H. J. *Phys. Rev. B* **1989**, *40*, 3685–3693.
101. Schmidt, A. J.; Collins, K. C.; Minnich, A. J.; Chen, G. *J. Appl. Phys.* **2010**, *107*, –.
102. Shin, S.; Kaviany, M.; Desai, T.; Bonner, R. *Phys. Rev. B* **2010**, *82*, 081302.